Geochemistry Geophysics Geosystems G3

Article
Volume 14, Number 8
6 August 2013
doi: 10.1002/ggge.20143
ISSN: 1525-2027

Published by AGU and the Geochemical Society

A rootless rockies—Support and lithospheric structure of the Colorado Rocky Mountains inferred from CREST and TA seismic data

Steven M. Hansen and Ken G. Dueker
Department of Geology and Geophysics, University of Wyoming, Laramie, Wyoming, USA

Now at Cooperative Institute for Research in Environmental Sciences, University of Colorado at Boulder, Boulder, Colorado, USA (steven.hansen@colorado.edu)

Josh C. Stachnik
Earth and Environmental Sciences Department, Lehigh University, Bethlehem, Pennsylvania,USA

Richard C. Aster
Geophysical Research Center and Department of Earth and Environmental Science, New Mexico Institute of Mining and Technology, Socorro, New Mexico, USA

Karl E. Karlstrom
Department of Earth and Planetary Sciences, University of New Mexico, Albuquerque, New Mexico, USA

[1] Support for the Colorado high topography is resolved using seismic data from the Colorado Rocky Mountain (CRM) Experiment and Seismic Transects. The average crustal thickness, derived from *P* wave receiver function imaging, is 48 km. However, a negative correlation between Moho depth and elevation is observed, which negates Airy-Heiskanen isostasy. Shallow Moho (<45 km depth) is found beneath some of the highest elevations, and therefore, the CRM are rootless. Deep Moho (45–51 km) regions indicate structure inherited from the Proterozoic assembly of the continent. Shear wave velocities from surface wave tomography are mapped to density employing empirical velocity-to-density relations in the crust and mantle temperature modeling. Predicted elastic plate flexure and gravity fields derived from the density model agree with observed long-wavelength topography and Bouguer gravity. Therefore, low-density crust and mantle are sufficient to support much of the CRM topography. Centers of Oligocene volcanism, e.g., the San Juan Mountains, display reduced crustal thicknesses and lowest average crustal velocities, suggesting that magmatic modification strongly influenced modern lithospheric structure and topography. Mantle velocities span 4.02–4.64 km/s at 73–123 km depth, and peak lateral temperature variations of 600°C are inferred. *S* wave receiver function imaging suggests that the lithosphere-asthenosphere boundary is 100–150 km deep beneath the Colorado Plateau, and 150–200 km deep beneath the High Plains. A region of negative arrivals beneath the CRM above 100 km depth correlates with low mantle velocities and is interpreted as thermally modified/metasomatized lithosphere resulting from Cenozoic volcanism.

Components: 14,967 words, 11 figures, 1 table.

Keywords: receiver functions; surface waves; Colorado Rocky Mountains; topographic support; lithosphere-asthenosphere boundary; Cenozoic volcanism.

Index Terms: 7218 Seismology: Lithosphere, 7203 Body waves, 7270 Tomography, 8138 Tectonics: Lithospheric flexure, 8178 Tectonics and magmatism.

Received 9 January 2013; **Revised** 29 March 2013; **Accepted** 8 April 2013; **Published** 6 August 2013.

Hansen, S. M., K. G. Dueker, J. C. Stachnik, R. C. Aster, and K. E. Karlstrom (2013), A rootless rockies—Support and lithospheric structure of the Colorado Rocky Mountains inferred from CREST and TA seismic data, *Geochem. Geophys. Geosyst., 14*, 2670–2695, doi:10.1002/ggge.20143.

1. Introduction

[2] The Earthscope transportable array (TA) has provided unprecedented seismic data coverage, and the tomography models resulting from this data have placed important constraints on the seismic structure of the upper mantle beneath the continental United States. [e.g., *Schmandt and Humphreys*, 2010; *Obrebski et al*., 2011]. However, the coarse 70 km station spacing is suboptimal for the purpose of scattered wave imaging, and the TA has been generally unable to provide robust high-resolution images above ~200 km depth, leaving key questions about the evolution and lithospheric structure of the continent unresolved. Of particular interest are the crust-mantle boundary (Moho) and the lithosphere-asthenosphere boundary (LAB) determined using the receiver function method. Current results from the TA are broadly consistent and show similar large-scale features, e.g., thinner crust and shallower LAB beneath the Basin and Range; however, significant discrepancies are observed in the small-scale structure where interpreted Moho depths may differ by up to ~10 km and LAB depths up to ~50 km [*Gilbert*, 2012; *Kumar et al*., 2012; *Levander and Miller*, 2012]. Similar discrepancies are observed in the short-wavelength structure between tomography models [*Becker*, 2012], highlighting the continued importance of dense-targeted seismic deployments.

[3] The purpose of this paper is to report on seismic results from the Colorado Rocky Mountain (CRM) Experiment and Seismic Transects (CREST) project, which recorded data from 59 Program for Array Seismic Studies of the Continental Lithosphere (PASSCAL) seismometers deployed for 15 months (2008–2009) in Colorado. This seismic experiment was spatiotemporally coincident with TA recordings and three permanent stations (Figure 1). The ~17 km mean station spacing provides a twofold to fourfold increases in spatial fold with respect to the TA, and these data, in conjunction with geologic studies [*Karlstrom et al*., 2012], are able to resolve controversies about the lithospheric structure and evolution of the highest topographic region in the continental United States, the CRMs.

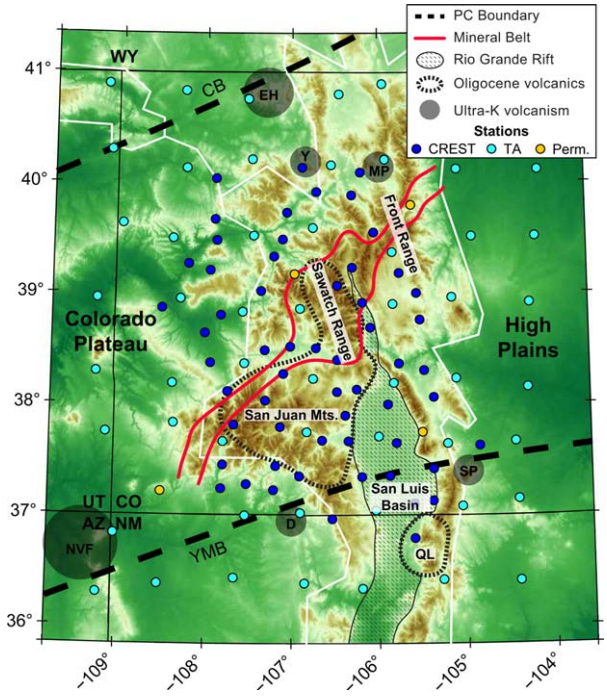

Figure 1. Annotated topographic map of the CRM region and surrounding regions. Seismic stations used in this study are denoted by colored circles: Earthscope TA, CREST array, and permanent stations (Perm.) from the U.S. and Intermountain West (IW) networks. Physiographic province boundaries are shown in white. Red lines denote the boundary of the Colorado Mineral Belt [from *Chapin*, 2012]. Dashed lines show the inferred locations of the Cheyenne Belt (CB) and Yavapai-Mazatzal boundary (YMB) from *Bennett and DePaolo* [1987]. Regions containing exposed calderas and plutons associated with Oligocene ignimbrite volcanism [*Lipman*, 2007] are shown by dashed lines. These include volcanic centers in the Sawatch Range, the San Juan Mountains, and the Questa-Latir area (QL). Shaded circles denote Cenozoic ultrapotassic rocks emplaced in the Elkhead Mountains (EH), Yampa (Y), Middle Park (MP), the Navajo Volcanic Field (NVF), Dulce (D), and Spanish Peaks (SP).

2. Geologic Setting

[4] The CRMs occupy a transitional region between the tectonically active Western United States and the stable North American craton. Since the late Cretaceous, this region has risen from sea level to an average elevation of about 3 km; the zenith of a long-wavelength (~1000 km) epeirogenic swell and the largest regional-scale topographic anomaly in North America [*Eaton*, 2008]. This N-S trending feature cuts across the grain of ancient structural features, including northeast trends associated with the Proterozoic accretion of the Colorado Province [*Reed et al*., 1987; *Whitmeyer and Karlstrom*, 2007] and northwest trends associated with the formation of the Ancestral Rocky Mountains [*Kluth and Coney*, 1981]. In addition to their topographic prominence, the CRM displays a long-wavelength Bouguer gravity low reaching −330 mGal, elevated surface heat flow up to 100 mW/m^2 [*Decker*, 1995; *Reiter*, 2008], and reduced seismic velocities in the crust and upper mantle [e.g., *Schmandt and Humphreys*, 2010; *Shen et al*., 2013]. Thermochronologic data indicate a multistage uplift history of this region [e.g., *Landman and Flowers*, 2013] that includes voluminous magmatism in the middle Cenozoic [*Roy et al*., 2004] followed by a pulse of Neogene uplift in this region [*Karlstrom et al*., 2012]. The latter is additionally supported by incision of post-Laramide sediments [*Leonard*, 2002; *McMillan et al*., 2006], anomalous areal extent, and postdepositional tilting of Neogene gravels [*Heller et al*., 2003; *McMillan et al*., 2002], and river geomorphology [*Karlstrom et al*., 2012; *Riihimaki et al*., 2007]. In total, these observations highlight the importance of middle to late Cenozoic processes in the development of this region.

[5] Since the late Mesozoic, the geologic history of the CRM has been dominated by the distant plate margin of western North America. The Laramide orogeny (75–45 Ma) is the most recent period of contraction and strongly influenced the physiography of the modern Rocky Mountains. Laramide structures record 10%–15% regional shortening, which is manifested locally by basement cored uplifts [*Erslev*, 1993] that are interpreted to be the result of compressional stresses transmitted to the lithosphere during flat-slab subduction of the Farallon plate [e.g., *Coney and Reynolds*, 1977]. Accompanying this shortening is the initial development of the Colorado Mineral Belt at ~75 Ma [e.g., *Chapin*, 2012], a northeast striking magmatic lineament extending from the western San Juan Mountains to the Front Range (Figure 1). The enigmatic Mineral Belt punctuates the Laramide volcanic gap, and its origin has been proposed to relate to the geometry of the Farallon plate at this time [*Chapin*, 2012; *Jones et al*., 2011], resulting in magmatic rejuvenation of Proterozoic shear zones [*Tweto and Sims*, 1963].

[6] Following Laramide flat-slab subduction, the Oligocene ignimbrite flare-up (38–23 Ma) resulted in the emplacement of numerous caldera complexes, the largest of which is located in the San Juan Mountains (Figure 1) and required the input of large volumes of mantle-derived basalts [*Farmer et al*., 2008; *Johnson*, 1991; *Lipman*, 2007]. Recently termed the Southern Rocky Mountain volcanic field, this feature is comparable in scale to the Altiplano-Puna volcanic complex in the central Andes, suggesting the development of a continental arc system in Colorado and New Mexico at this time [*Lipman*, 2007; *Chapin et al*., 2004]. Alternatively, it has been proposed that melting of hydrated mantle lithosphere following removal of the Laramide flat slab is responsible for the ignimbrite flare-up [*Humphreys et al*., 2003]. However, in the San Juan Mountains, this would require focusing melts generated over distances of hundreds of kilometers [*Farmer et al*., 2008]. Minor episodic extension and mafic volcanism associated with the Rio Grande rift system occurred following the main pulse of Oligocene volcanism. Rifting is expressed in the CRM region by a narrow series of asymmetric grabens in the San Luis, Upper Arkansas, and Blue River valleys (Figure 1), and by diffuse extensional faulting that extends into northern Colorado and southern Wyoming [*Baldridge et al*., 1995; *Berglund et al*., 2012; *Ingersoll*, 2001; *Keller et al*., 1991; *Landman and Flowers*, 2013; *Tweto*, 1979].

3. Topographic Support

[7] The compensation mechanisms responsible for supporting the high topography of the CRM remain contentious, and a detailed accounting of lithospheric buoyancy has yet to be performed. Previous receiver function analysis has determined that the crust beneath the Rocky Mountains is thicker on average than the Basin and Range province. However, the high topography lacks thickened crust relative to the adjacent and lower-standing High Plains, suggesting that the CRM are partially supported by low-density upper mantle

[*Gilbert and Sheehan*, 2004; *Lee and Grand*, 1996; *Sheehan et al*., 1995]. This interpretation is supported by thermal modeling of mantle velocities and attenuation, which indicates elevated temperatures beneath the CRM [*Boyd and Sheehan*, 2005; *Goes and van der Lee*, 2002; *Lee and Grand*, 1996]. Additionally, some tomography-based mantle convection models for the western United States predict ~1 km of present-day dynamic topography for the Colorado Plateau, declining eastward to 100–500 m of uplift across the CRM [*Forte et al*., 2010; *Liu and Gurnis*, 2010; *Moucha et al*., 2008]. Small-scale convection has also been proposed in this region [*van Wijk et al*., 2010] and may be affecting the current CRM topography [*Coblentz et al*., 2011].

[8] In contrast with these findings, several studies attribute the high topography to shallow density variations. Reduced crustal shear wave velocities derived from surface wave analysis were used to argue for support, resulting solely from low-density crust [*Li et al*., 2002]. Density modeling of seismic velocities determined from joint inversion of surface wave and receiver function data suggests that the observed Bouguer gravity field in this region is inconsistent with significant density variation below 50 km depth [*Bailey et al*., 2012]. Finally, analysis of elevation and geoid data indicates that the buoyancy supporting the high topography resides above 100 km depth [*Coblentz et al*., 2011]. Therefore, the relative importance of buoyant crust, buoyant mantle, and dynamic mantle flow in supporting the high topography remains uncertain.

4. Data and Methods

[9] In this study, we investigate the seismic structure of the crust and upper mantle beneath the CRM region with an emphasis on the support mechanisms that distinguish the high-standing topography from the neighboring Colorado Plateau and High Plains, which are 0.7–1.0 km lower in mean elevation. The geologic events that have affected this region are interpreted to infer the age and origin of the observed seismic structures. Crustal thickness variations beneath the CREST array are measured from a *P* wave receiver function image volume. Negative velocity gradients in the uppermost mantle are constrained from *S* wave receiver function imaging. Isotropic shear wave velocities are determined via tomographic inversion of ambient and earthquake surface wave phase velocity measurements. Subsurface densities are estimated from the resulting velocity model, utilizing empirical velocity-to-density scalings in the crust and anelastic temperature modeling in the mantle. The efficacy of Airy-Heiskanen and Pratt-Hayford isostatic models in support of the CRM high topography is investigated using the observed Moho depths and modeled crustal densities. Finally, the flexural response of the lithosphere and Bouguer gravity are calculated from the combined crust and mantle density models. These results are compared with observed topography and Bouguer gravity fields to produce a unified geophysical view of lithospheric structure and topographic support for the CRM.

4.1. Scattered Wave Imaging

[10] The receiver function methodology is applied to teleseismic body-wave recordings to isolate *P*-to-*S* and *S*-to-*P* converted arrivals, henceforth denoted as P_s and S_p, respectively. The initial data set consists of three-component traces windowed about theoretical *P* and *S* wave arrival times for global events with a body-wave magnitude greater than 5.7. The *P* wave data set consists of direct arrivals from 30°–100° epicentral distance. The *S* wave data set consists of direct *S* arrivals from 55°–84° and SKS arrivals from 84°–120° distance. These data are visually culled to remove noisy traces, identify any misoriented or polarity-reversed seismogram components, and delete events with a poor signal-to-noise ratio. Travel-time residuals are measured, and the waveforms are aligned for each event using a multichannel cross-correlation algorithm [*VanDecar and Crossen*, 1990].

[11] *S* wave receiver functions are superior to *P* wave receiver functions for investigating mantle velocity structure between the Moho and 200 km depth because the two primary free-surface Moho reverberations interfere with direct P_s arrivals from discontinuities within this depth range [e.g., *Kind et al*., 2012]. However, *S* wave receiver functions introduce additional data-processing complexities. Careful data culling and time windowing are required to avoid contamination by secondary *S* wave arrivals near the 84° S-SKS crossover distance [*Wilson et al*., 2006; *Yuan et al*., 2006]. Prior to deconvolution, the culled *S* wave traces are time-reversed to account for the precursory nature of S_p scattering. Polarities of the resulting receiver functions also need to be reversed to account for the sign difference between S_p and P_s conversions.

[12] The *P* and *S* wave receiver functions are calculated using a multichannel deconvolution

algorithm that consists of three steps. First, the source function amplitude spectrum for each event is approximated using a rough-smooth spectral separation algorithm [*Hansen and Dueker*, 2009]. Second, the three-component receiver function amplitude spectrum is calculated via least-squares inversion using the source spectral estimates as constraints. Finally, the receiver function spectral phase is reconstructed by exploiting the minimum-phase nature of the direct-component trace. The details of this methodology are presented elsewhere [*Baig et al.*, 2005; *Bostock*, 2004; *Mercier et al.*, 2006], and the application to temporary array recording and *S* wave data was demonstrated by Hansen and Dueker [2009]. We note several advantages afforded by this approach. A single source function is estimated from all stations recording a particular event as opposed to using individual direct-component traces [e.g., *Helffrich*, 2006; *Ligorria and Ammon*, 1999], which record site-specific effects and pure-mode scattering, e.g., P_p and S_s. Redundant Earth structure sampling due to earthquake source region clustering is exploited by binning the events recorded at each station by distance and backazimuth. The data are then simultaneously deconvolved to estimate a single three-component receiver function for each station-event bin.

[13] The resulting *P* and *S* wave receiver functions are band-pass filtered at 1–10 s and 3–20 s period, respectively. Filtered data are statistically culled to delete noisy and unusably narrow-band traces using three quality criteria: root mean square value, maximum amplitude, and the maximum to mean ratio of the amplitude spectrum. Traces with any criterion outside of the 95th percentile are discarded, which resulted in a total of 3708 and 2238 *P* and *S* wave receiver functions.

[14] Traces are mapped from time to space by tracing *P* and *S* wave rays through our three-dimensional surface wave tomogram described in the next section. Crustal *P* wave velocities are estimated by scaling the shear wave model with a two-dimensional V_p/V_s field. Estimates of crustal V_p/V_s were derived from stacking the *P* wave receiver function data along V_p/V_s and crustal thickness-dependent moveout curves [*Zhu and Kanamori*, 2000]. The stacks are visually culled to remove spurious results and the culled data are interpolated and smoothed with a Gaussian filter (Figure 2). Below the Moho, an uppermost mantle V_p/V_s ratio of 1.81 is assumed, as determined from the AK135 reference earth model [*Kennett et al.*, 1995]. Velocities along the calculated raypaths are

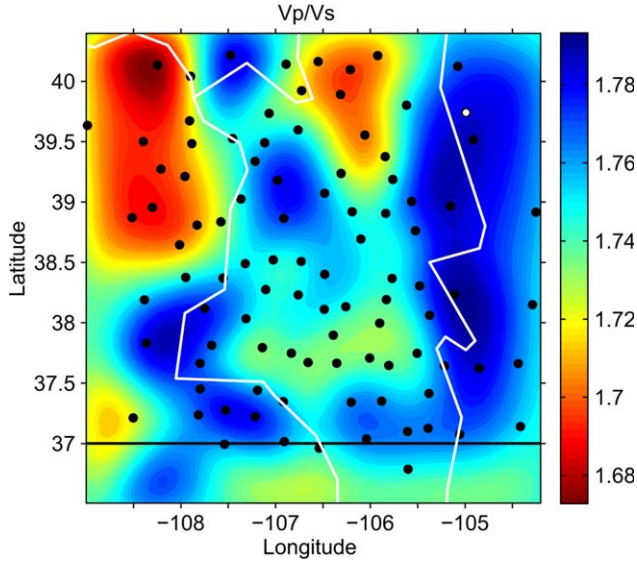

Figure 2. V_p/V_s ratio map resulting from stacking of individual station *P* wave receiver function data. SV-component receiver functions are stacked along moveout curves calculated for the direct Moho arrival and the free-surface Moho reverberations 2P1S. P-component receiver functions are stacked along the 3P Moho reverberation curve. The array-averaged V_p/V_s ratio is 1.75.

used in the one-dimensional moveout equation to map time to depth, and the results are stacked via the common conversion point (CCP) method [*Dueker and Sheehan*, 1997] to produce velocity images. Subsurface image points are spaced 1 km vertically, and are spaced 8 and 14 km laterally for the *P* and *S* wave data, respectively. The traces contributing to each image point stack are collected from lateral bins that are 56 and 126 km wide for the respective *P* and *S* wave data set s.

[15] Moho depths are measured from the *P* wave image volume via a semiautomated algorithm involving two steps. First, initial picks are made automatically by locating local maxima at each model offset between 35 and 65 km depth. Second, depth picks are plotted on image cross sections and visually inspected for accuracy. Continuity of the Moho is used to determine the correct arrival in regions where multiple picks are present, and spurious or ambiguous picks are removed. The culled Moho depths are then interpolated and laterally smoothed using a two-dimensional Gaussian function with a 47 km half width.

4.2. Surface Wave Tomography

[16] Short-period (5–35 s) fundamental-mode Rayleigh wave phase velocities are derived from the

ambient noise field in a three-step process using the stations shown in Figure 1. First, time-windowed continuous waveform data are filtered, spectrally whitened, cross correlated, and stacked to estimate the empirical interstation Green's functions [e.g., *Bensen et al*., 2007; *Shapiro and Campillo*, 2004]. Second, phase velocities are measured by fitting the zero crossings of the real cross spectra with Bessel functions of the first kind, which stabilizes measurements for stations separated by less than one wavelength [*Aki*, 1957; Ekström *et al*., 2009]. Finally, phase velocity maps are produced with 20 km square grid cells using ray theory and an iteratively reweighted least-squares tomographic inversion with model norm damping [*Stachnik*, 2010; *Stachnik et al*., 2008]. Long-period (35–80 s) phase velocity maps calculated via Eikonal tomography [*Lin and Ritzwoller*, 2011] using CREST and TA stations (Figure 1) are incorporated to constrain the deeper structure (W. Shen, personal communication).

[17] The three-dimensional shear wave velocity structure is estimated by jointly inverting the earthquake- and ambient noise-derived phase velocity maps onto a uniform grid with 20 km spacing. An iterative least-squares solver is implemented to calculate one-dimensional velocity profiles at each node [*Herrmann and Ammon*, 2002] with equal weighting between the two phase-velocity data set s. The starting model is constant at 4.4 km/s and is parameterized by 2 km thick layers down to 50 km depth, increasing to 5 km and then 10 km at 120 km depth. The resulting models are spline interpolated in depth and laterally smoothed with a 40 km half width Gaussian function to produce the final three-dimensional velocity model. Inverse regularization parameters chosen from values near the "elbow" observed in L-curve analysis [e.g., *Aster et al*., 2012] and checkerboard tests at 100 km depth are shown in Figure 3.

4.3. Density and Temperature Modeling

[18] The density structure to 170 km depth is estimated from the surface wave tomogram assuming that, to first order, velocity modulation is attributable to compositional variations in the crust and to temperature differences in the mantle. Density values in the upper crust (<10 km depth) are calculated using the V_s-V_p and V_p-density regressions from *Brocher* [2005], which are based on a compilation of measurements at near-surface conditions. Pressure and temperature effects need to be accounted for at greater depths, but there has been little work relating crustal V_s to density at these conditions, and there is no obvious empirical relation between V_p/V_s and density [*Christensen*, 1996]. For these reasons, compressional wave velocities in midcrust to Moho depths are first estimated by scaling the modeled shear wave velocities by the array-averaged V_p/V_s ratio of 1.75 (Figure 2), and then the nonlinear depth-dependent fits from *Christensen and Mooney* [1995] are applied to calculate density. These regressions are based on laboratory measurements of density and V_p performed on a variety of crystalline lithologies at relevant pressures (10–50 km depth); velocities were temperature corrected to an average geotherm. Lateral temperature variations in the crust have been ignored in this approach and may result in density errors of up to ~7% per 100°C at 30 km depth.

[19] Temperature variations affect observed mantle shear wave velocities via both anharmonic and anelastic thermal effects [*Karato*, 1993]. These variations are calculated from the *Jackson and Faul* [2010] extended Burgers representation of olivine anelasticity. This model is thought to account for grain boundary sliding and has good laboratory control but requires extrapolating pressure and grain size effects. Velocities at each model depth are mapped to temperature by interpolating the numerically evaluated frequency and pressure-dependent temperature-velocity curves with an assumed grain size of 1 mm (see section 6). The dominant surface wave period at each model depth is approximated using a linear relation to account for the frequency dependence of surface-wave sensitivity kernels. Mantle density perturbations are calculated by scaling the temperature differences relative to an adiabatic geotherm with the thermal expansion coefficient model for Phanerozoic lithosphere from *Afonso et al* . [2005]. The geotherm and reference density column are calculated [*Turcotte and Schubert*, 2002] with a 1400°C mantle potential temperature [*Putirka*, 2008].

4.4. Flexure and Gravity Modeling

[20] Surface topography is predicted from the density model, which includes crustal thickness variations and crust and upper mantle lateral density differences. Static mechanical equilibrium requires that spatial variations in subsurface buoyancy are balanced by topographic loading and by forces arising from flexure of the lithosphere, which is modeled as a two-dimensional elastic plate under the assumption of pure elastic

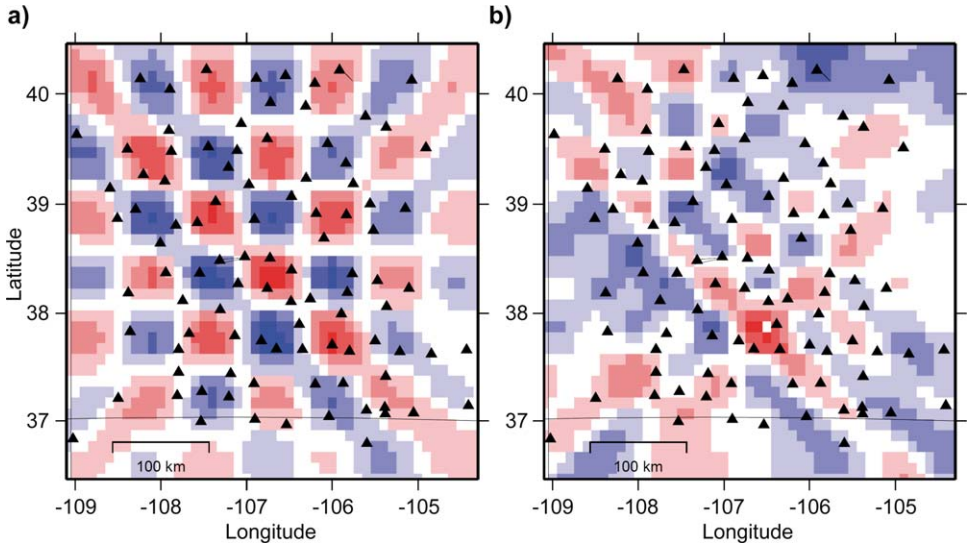

Figure 3. Checkerboard resolution test for ambient noise tomography at 25 s period. Input model is alternating positive (blue) and negative (red) anomalies with unity amplitude. Resulting model is shown for (a) 75 km square checkers and (b) 50 km square checkers. Spatial recovery of checkers is very good, particularly given that checkerboard tests represent extreme distribution of anomalies and can be difficult to interpret. Maximum amplitude recovery for both Figures 3a and 3b is 15%, shown in identical color scales.

coupling. Flexural topography is calculated in the Fourier domain by applying a two-dimensional elastic plate filter to the distributed buoyancy load, where the load is calculated from vertical integration of the density model (Appendix A). Plate strength is assumed to be homogeneous, and the optimal elastic thickness is determined by minimizing the misfit between the predicted flexure and observed topography (Figure A2). The effects of viscous coupling have been ignored in this approach and could potentially overestimate topographic effects of the deep density structure [e.g., *Hager and Richards*, 1989].

[21] The density and flexure modeling accuracy is tested by comparing these results with gravity and topography data. Over 65,000 terrain-corrected Bouguer gravity measurements for this region were obtained from the Pan-American Center for Earth and Environmental Studies (PACES) U.S. gravity database [*Keller et al*., 2006]. Bouguer gravity at each surface location is predicted from the density model by first calculating the vertical gravitation due to each model block with the analytic solution for a rectangular prism [*Nagy et al*., 2000], which reduces near-surface discretization effects. Numeric volume integration is then performed to obtain total gravitation.

5. Results

5.1. Crustal Structure

[22] Cross sections through the *P* wave receiver function image volume (Figure 4) display a well-defined Moho arrival beneath most of the array at 40–51 km depth below mean sea level. Image quality degrades outside the CREST array footprint due to reduced TA data fold. Additionally, the image becomes energetic beneath the ~3 km thick low-velocity sedimentary rocks in the San Luis Basin [*Brister and Gries*, 1994] presumably due to free-surface basin reverberations (Figure 4f south of 37.5°). A Moho depth map derived from these results is shown in Figure 4g. The shallowest Moho is observed in northern New Mexico beneath the southern San Luis Basin of the Rio

Table 1. Province Averaged Elevation and Seismological Observables From the CREST Array[a]

Province	Elevation (km)	Moho Depth (km)	Crustal Thickness (km)	Crustal V_s (km/s)	Mantle V_s (km/s)
CRM	2.84 (0.45)	44.6 (1.77)	47.3 (1.72)	3.51 (0.24)	4.28 (0.14)
CP	2.15 (0.40)	46.4 (2.01)	48.6 (1.92)	3.60 (0.32)	4.33 (0.12)
HP	1.86 (0.32)	46.1 (2.20)	48.1 (2.10)	3.59 (0.32)	4.35 (0.13)

[a]CRM, Colorado Rocky Mountains; CP, Colorado Plateau; HP, High Plains.

Grande rift (40 km) and the deepest Moho is found in northwest Colorado (51 km).

[23] A comparison of physiographic province Moho depths (Table 1) shows that the CRM crust is 0.8–1.3 km thinner on average than the Colorado Plateau and High Plains. Notably, the 0.7–1 km of excess CRM topography is not supported by thickened crust as the Moho is about 2 km shallower with respect to the adjacent provinces. Significant short-wavelength heterogeneity is observed in the Moho depth map (Figure 4g), which is not captured by the province-averaged values. Within the CRM, the Moho is typically observed at less than 45 km depth, except beneath the Front Range and near the Colorado-New Mexico border where deeper Moho depths are found (45–49 km). Noteworthy is that Moho depths beneath much of the high topography, particularly the San Juan Mountains, are up to 2 km shallower than the CRM province mean.

[25] This result is further illustrated in the elevation versus Moho depth histogram (Figure 5), which displays a negative correlation ($R = -0.46$) showing that the highest elevations are associated with some of the thinnest crust in Colorado. This observation is in stark contrast to the positive trend predicted by Airy-Heiskanen isostatic compensation (*Watts*, 2001) and leads to our terminology of a "rootless Rockies." The measured Moho depths are affected by the laterally varying V_p/V_s model (Figure 2) used to estimate crustal P wave velocities for the CCP imaging; however, a similar negative correlation between Moho depth and elevation is observed if a constant V_p/V_s ratio is applied, indicating that this result is robust.

[26] Depth-averaged surface wave tomography and density modeling results (Figure 6) indicate that the CRMs have reduced crustal velocities and densities relative to the Colorado Plateau and High Plains (Table 1). Average crustal shear wave velocity in the CRM is 3.51 km/s and lowest velocities (3.45–3.53 km/s) are observed along an N-S trend in the western CRM (Figure 6a). This trend extends south from the Sawatch Range, to a broad region encompassing the San Juan Mountains, and

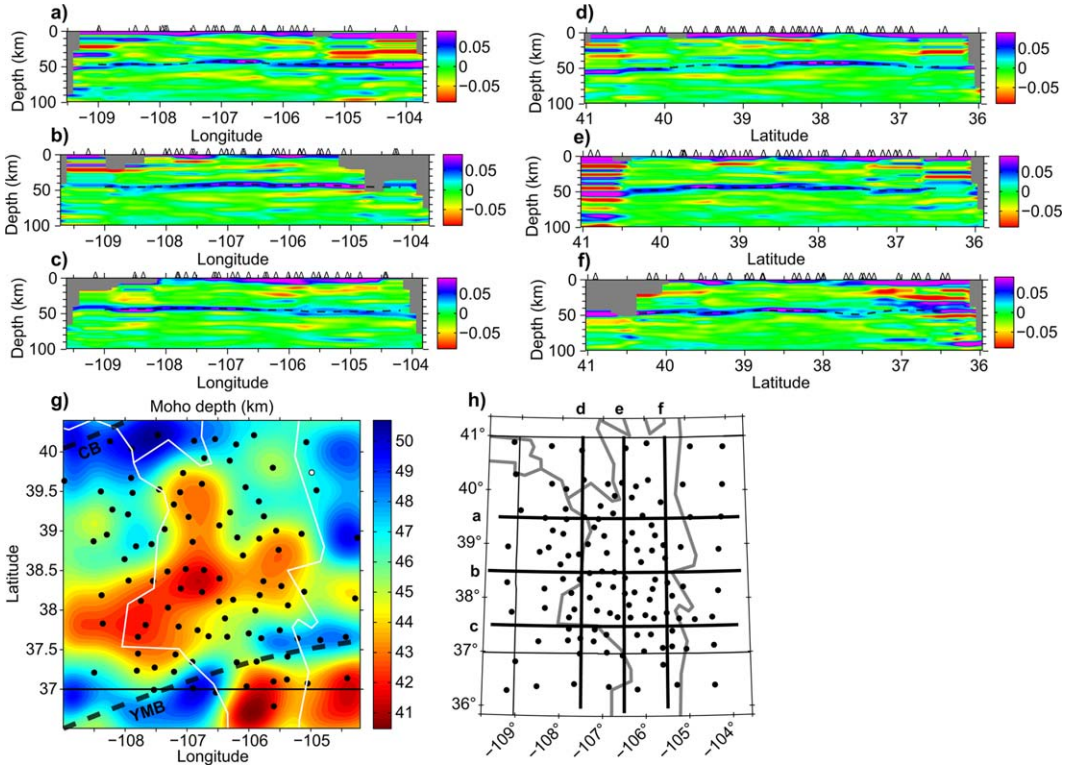

Figure 4. *P* wave receiver function image results. Cross sections striking (a–c) E-W and (d–f) N-S. Station locations are shown by triangles and regions without data are shaded gray. Color bars denote the stacked receiver function amplitudes, which are normalized to the amplitude of the direct arrival. The smoothed Moho picks are plotted as dashed lines. (g) The resulting Moho depth map. Lines denoting Proterozoic crustal boundaries (Figure 1) are plotted. Station locations are shown by black circles and physiographic province boundaries are displayed in white. (h) Cross section locations are depicted.

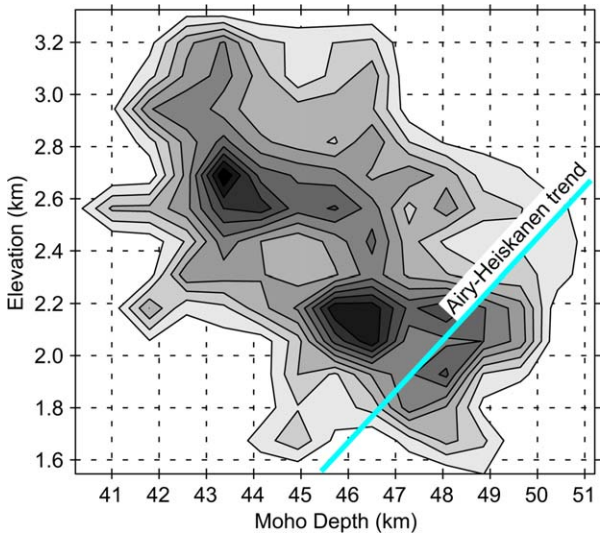

Figure 5. Two-dimensional histogram of Moho depth versus elevation. The trend predicted by Airy-Heiskanen isostasy is labeled and was calculated using the average modeled density for the crust (2.52 g/cm^3) and the PREM density model as a reference column.

to the San Luis Basin near the Questa-Latir Peaks area (Figure 1). The lowest average crustal velocity (3.45 km/s) and density (2.74 g/cm^3) values are observed beneath the eastern San Juan Mountains.

[27] A strong negative correlation ($R = -0.86$) is observed between elevation and mean crustal density, similar to that predicted by Pratt-Hayford isostatic compensation (Figure 6c). This observation suggests that the high topography is in part compensated by a low-density crust. However, the observed Moho depths are inconsistent with pure Pratt-Hayford compensation because the density-elevation data predict Moho depths ranging between 46 and 54 km (Figure 6c).

5.2. Mantle Velocity and Temperature

[28] Depth-averaged mantle shear wave velocities (Figure 6b) range from 4.23 to 4.45 km/s and, similar to the crust, a region of slow velocities is observed beneath the CRM. The lowest mean upper mantle velocities (4.23–4.26 km/s) are observed beneath the San Luis Basin near the New Mexico-Colorado border, and the highest velocities (4.38–4.45 km/s) are located in northwest Colorado and beneath the High Plains and Front Range (Figure 6b). Individual depth slices (Figures 7a–7c) reveal greater short-wavelength heterogeneity and lateral velocity variations reaching ±5%.

[29] Temperatures inferred from thermal modeling of mantle velocities (Figure 7) range from 670° to 1410°C and peak lateral thermal variations reach ~600°C. With an assumed 1 mm olivine grain size, the temperature model below 50 km depth does not exceed either the dry peridotite solidus [*Hirschmann*, 2000] or the assumed 1400°C mantle adiabat [*Putirka*, 2008]. Velocities directly beneath the Moho are typically too slow to be modeled by realistic temperatures but are most likely affected by tomographic smearing of lowermost crustal velocities because a Moho velocity step is not resolvable in the surface wave tomography. Between 73 and 123 km depth, province-averaged temperatures (Figure 7d) increase quasi-linearly with depth and the thermal gradient increases from east to west across the CRM.

[30] At 73 km depth (Figure 7a), the highest inferred temperatures (1150°C–1270°C) are located beneath the CRM, which is clearly distinct from the colder upper mantle of the High Plains and Colorado Plateau (670°C–1000°C). Temperature differences between the plateau and the CRM mantle decrease with depth, and asthenosphere-like temperatures (>1300°C) are reached beneath much of this region at 123 km depth (Figures 7b–7c). In contrast, a high-velocity/low-temperature region persists downward through all model depths beneath the Front Range and High Plains.

5.3. S_p Imaging

[31] Cross sections through the *S* wave receiver function image volume (Figure 8) display a prominent Moho arrival that is consistent with the Moho depths derived from the *P* wave receiver function image (Figure 4g). The image volume is dominated below the Moho by negative-polarity arrivals, the depths of which broadly correlate with physiographic province. These arrivals indicate the presence of negative velocity gradients, i.e., higher velocity over lower velocity, that occur over less than 20 km depth assuming an 8 s dominant period and half wavelength sensitivity [*Rychert et al.*, 2007]. Negative arrivals are imaged beneath the Colorado Plateau at 100–150 km depth and are spatially coincident with a negative velocity gradient observed in the surface wave tomogram (Figure 8). The CRM are associated with a broad band of negative polarity arrivals imaged at 60–110 km depth that extends laterally into both the Colorado Plateau and the High Plains region. The deepest negative arrivals are observed beneath the High Plains and eastern CRM at 150–200 km depth.

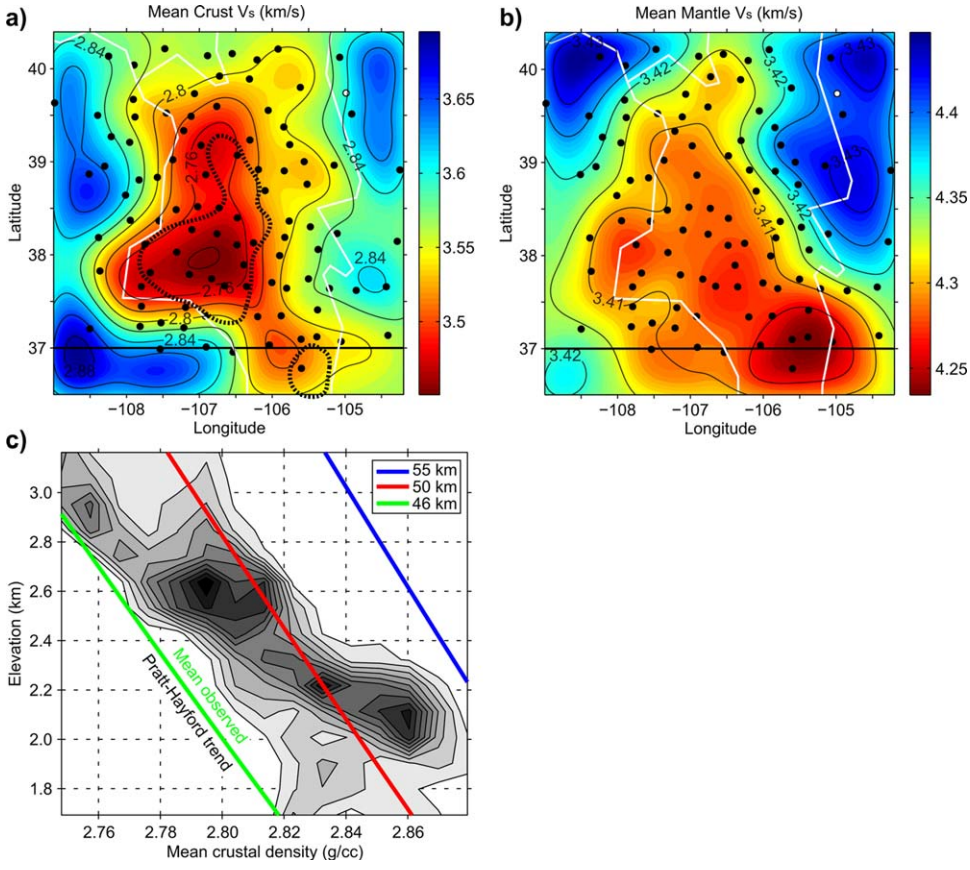

Figure 6. Surface wave tomography, density modeling, and Pratt-Hayford topographic compensation. (a) Average shear wave velocity of the crust overlain with contours depicting estimated mean crustal density with a spacing of 0.02 g/cm^3. Dashed lines denote Oligocene flare-up volcanic regions (Figure 1). (b) Mean shear wave velocity from the Moho to 170 km depth with estimated mean density contours with a spacing of 0.005 g/cm^3. (c) Elevation versus mean crustal density histogram; trends predicted by Pratt-Hayford isostasy for a range of Moho depths are shown and the array average Moho depth of 46 km (Figure 5) is labeled. Topography and averaged density and velocity data are laterally smoothed with the same Gaussian filter as the Moho depth map of Figure 4g.

5.4. Flexure and Gravity Modeling

[32] Elastic plate flexure predicted from the combined crust and mantle density models (Figure 9) displays a prominent N-S oriented ridge of elevated flexural topography along the western CRM. In this region, positive buoyancy resulting from reduced crust and mantle densities is larger than negative buoyancy associated with thinner crust (Figure A1). Maximum plate deflection is observed in the eastern San Juan Mountains, where peak differential topography of about 1.7 km is reached relative to the High Plains and Colorado Plateau. Contributions from CRM mantle buoyancy increases to the south and account for approximately half of the net flexural topography (Figure A1). The optimal elastic plate thickness determined from flexure modeling is 12 km (Figure A2), and the width of the main lobe in the resulting spatial filter response function is 200 km. This estimate is in good agreement with the <20 km estimate of *Coblentz et al*. [2011] and is on the low end of the broad range of values reported in other studies (10–60 km) [*Bechtel et al*., 1990; *Lowry et al*., 2000; *Lowry and Perez-Gussinye*, 2011].

[33] The flexure model accounts for 45% of the elevation variance, and cross sections show that the model successfully captures the general long-wavelength observed topography (Figures 9b–9d). The largest feature in the topography misfit (Figure A2a) is the anomalous Front Range, where observed elevations are consistently ∼1 km greater than flexure model predictions (Figure 9b east of −107°). The positive free-air gravity

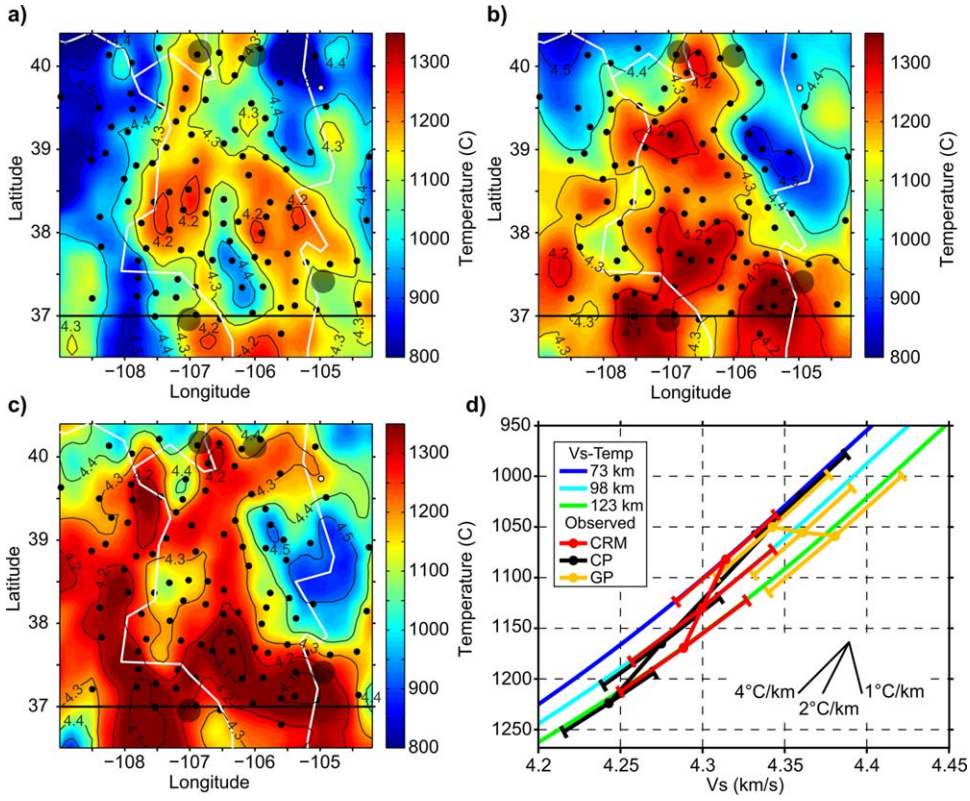

Figure 7. Map views of upper mantle shear wave velocity and modeled temperatures at (a) 73 km, (b) 98 km, and (c) 123 km depth. Temperature plots are overlain with contours showing shear wave velocities with a spacing of 0.1 km/s. Shaded circles denote occurrences ultrapotassic rocks (Figure 1). (d) Calculated velocity-temperature curves at each depth are overlain by the province averaged temperatures which are denoted by dots. The standard deviation of temperatures and velocities are plotted as error bars.

indicates that this region is uncompensated, but the spatial wavelength of the Front Range is too large to be elastically supported by a 12 km thick plate (Figure A2b). Previous studies have found heterogeneous elastic thickness in Colorado, and it is plausible that the lithosphere is significantly stronger beneath the Front Range (i.e., elastic thickness of 40–50 km) [*Lowry et al.*, 2000; *Lowry and Perez-Gussinye*, 2011]. This interpretation is also consistent with the cool mantle temperatures inferred from velocity modeling (Figure 7) which should strengthen the lithosphere [*Burov and Diament*, 1995].

[34] The Bouguer gravity field calculated from the density model (Figure 10) exhibits a large negative anomaly along the western CRM, displaying two distinct minima over the Sawatch Range and the San Juan Mountains. The San Juan minimum embodies a peak gravity reduction of 130 mGal with respect to the Colorado Plateau. Profiles comparing observed and predicted gravity (Figures 10c–10e) show that the density model is able to reproduce the long-wavelength features of the Bouguer field with a variance reduction of 60%. Largest misfits occur near the model periphery and can likely be attributed to edge effects resulting from decreased resolution of the surface wave tomogram and/or from density variations outside of the model domain that are not accounted for. The model also fails to capture shorter wavelength features of the observed gravity field, suggesting additional density and/or velocity heterogeneity in the shallow crust [*Lin et al.*, 2012], e.g., basin sediments.

6. Discussion

6.1. Topographic Support

[35] Mean crustal thickness beneath the CREST array is 48 km, which generally agrees with *P* wave receiver function results from the TA [*Gilbert*, 2012, *Levander and Miller*, 2012]. However, the CREST array provides two to four times the

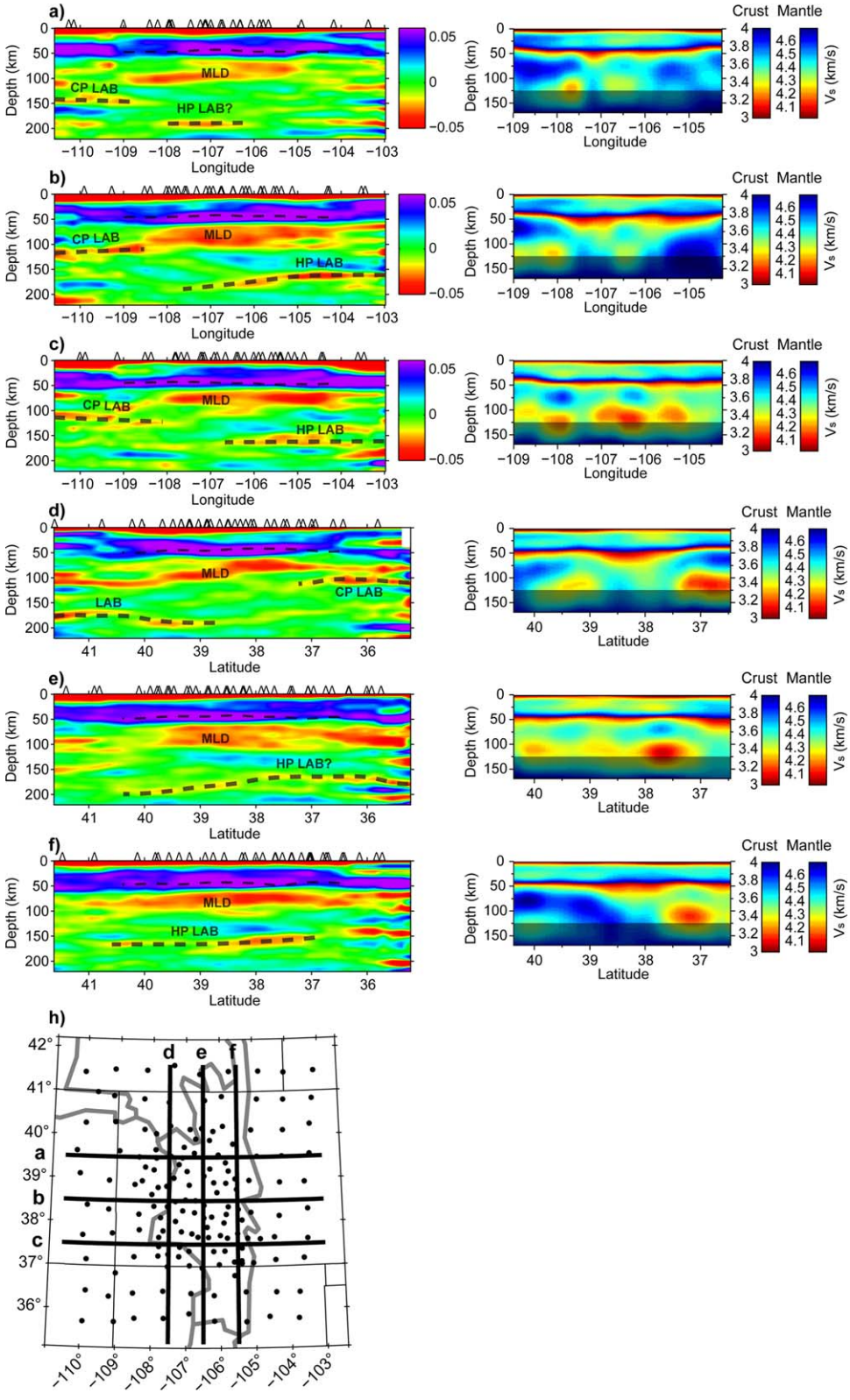

Figure 8. (a–c) E-W and (d–f) N-S trending cross sections through the (left) *S* wave receiver function image volume and the (right) surface wave tomography model. Moho depth picks are plotted as dashed lines on image sections above 50 km depth. The interpreted LAB beneath the High Plains (HP) and Colorado Plateau (CP) are labeled. The inferred shallow mid-lithosphere discontinuity (MLD) beneath the Rockies is labeled. (g) Cross-section locations (same as in Figure 4). Tomogram velocities are plotted from 3 to 4 km/s in the crust and from 4 to 4.65 km/s in the mantle as delineated by the Moho depths determined from the P_s imaging. Model resolution degrades below ~120 km depth and this region is shaded.

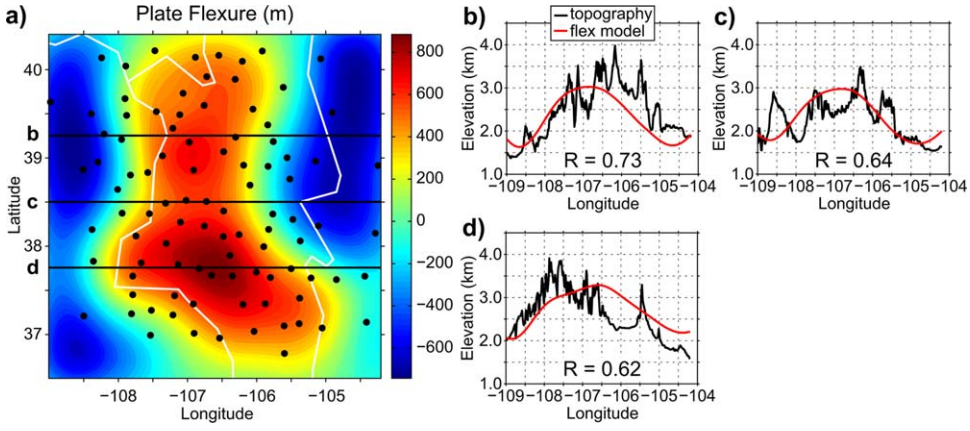

Figure 9. Elastic plate flexure modeling and observed topography. (a) Vertical plate deflection resulting from lateral buoyancy variations in the density model. An elastic thickness of 12 km is used. (b–d) E-W profiles comparing the flexure model and observed topography. Cross section locations are shown as black lines in Figure 9a and the correlation coefficients are shown.

spatial sampling with respect to these studies and places important additional constraints on the small-scale structure of this region. In particular, the TA studies were unable to resolve the thinner crust observed in this study beneath the high topography. Despite being nearly 7 km thicker with respect to average continental crust [*Christensen and Mooney*, 1995], only a weak negative correlation exists between topography and Moho depth (Figure 5). This analysis clearly negates Airy-Heiskanen compensation of the CRM high topography and further demonstrates that no simple relationship exists between crustal thickness and elevation [*Zoback and Mooney*, 2003].

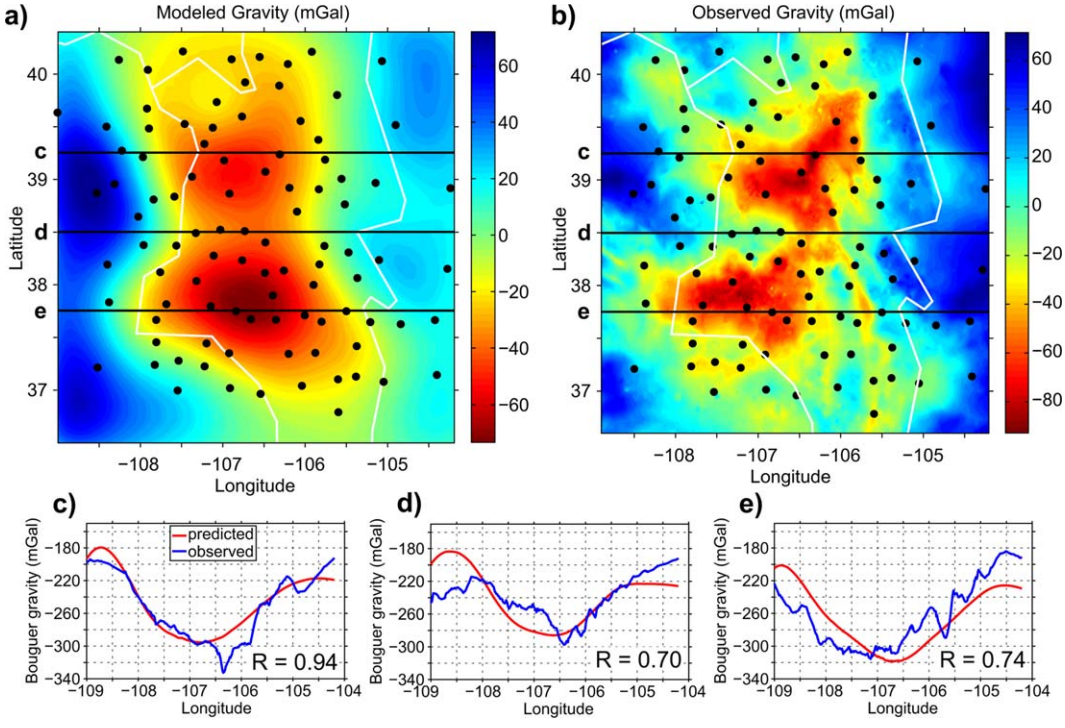

Figure 10. (a) The Bouguer gravity field calculated from the density model and (b) the measured Bouguer gravity from the PACES database. (c–e) E-W profiles comparing predicted and observed Bouguer gravity. Cross-section locations are shown in Figures 10a and 10b and the correlation coefficients are shown.

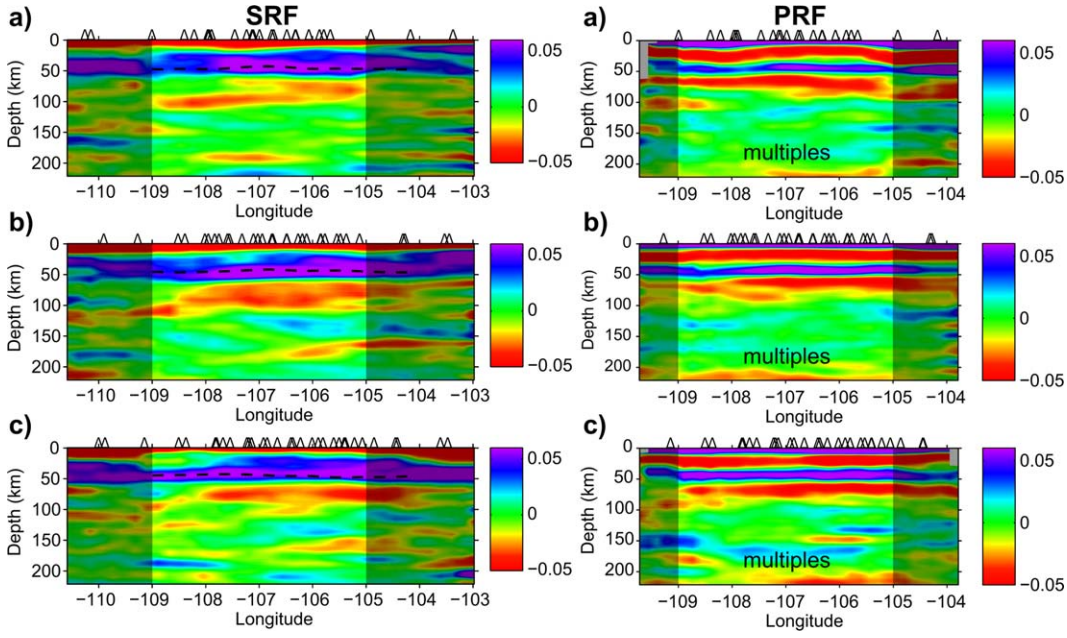

Figure 11. (a–c) A direct comparison of E-W trending image cross sections from *S* wave receiver function (SRF) and *P* wave function stacking (PRF). Low-fold regions at the array periphery are shaded. (g) Moho depth picks are plotted as dashed lines in the *S* wave sections. The region contaminated by free-surface Moho multiples is labeled in the *P* wave sections. Cross sections are at coincident latitudes and the locations are plotted in Figures 8g and 4h.

[36] Reduced velocities indicate the presence of low-density crust beneath the CRM high topography, and therefore, Pratt-Hayford compensation is a more viable support mechanism for this region (Figure 6). However, both isostatic end-member models neglect the effects of a finite strength lithosphere and upper mantle density variations (Figure 6b), which are evidenced by thermal modeling of tomogram velocities (Figure 7). Flexure modeling demonstrates that buoyancy resulting from a combination of low-density crust and elevated mantle temperature is sufficient to explain the excess topography of the CRM relative to the Colorado Plateau and High Plains (Figure 8). Therefore, no local mantle flow pressures associated with small-scale convection [*Coblentz et al.*, 2011; *van Wijk et al.*, 2010] are required to support the topography of the CRM. However, some form of advective heat/mass transfer is almost certainly required by the inferred mantle temperature variations which reach 600°C. It is important to note that our analysis is insensitive to topographic mean and any absolute elevation changes [e.g., *Karlstrom et al.*, 2012] as only the relative density differences are utilized for flexure modeling (Appendix A). Thus, any long-wavelength regional-scale dynamic topography [*Forte et al.*, 2010; *Liu and Gurnis*, 2010; *Moucha et al.*, 2008] is not considered here.

6.2. Precambrian Structure

[37] A striking correlation exists between the Moho depth map and the inferred surface locations of Precambrian crustal boundaries (Figures 1 and 4g), suggesting that structures left over from lithospheric assembly persist in the modern plate architecture. The deepest Moho observations in northwest Colorado are interpreted to be related to crustal shortening across the ~1.76 Ga Cheyenne Belt suture between the Proterozoic Colorado and the Archean Wyoming provinces [*Chamberlain*, 1998; *Karlstrom and Houston*, 1984]. This interpretation is consistent with results from the PASSCAL Lodore and Deep Probe seismic arrays at −109° longitude, the CD-ROM experiment at −107° and the Laramie array at −106°, which imaged crustal thicknesses exceeding 50 km beneath the suture zone [*Crosswhite and Humphreys*, 2003; *Hansen and Dueker*, 2009; *Morozova et al.*, 2005; *Snelson et al.*, 1998].

[38] Similarly, we interpret the E-NE trending lineament of thickened crust traversing southern Colorado and northern New Mexico as a crustal welt left from the suturing of the Proterozoic Yavapai and Mazatzal provinces [e.g., *Whitmeyer and Karlstrom*, 2007]. The location of the exact suture

is uncertain [see *Shaw and Karlstrom*, 1999], and other workers have suggested the main suturing occurred further south along the Jemez lineament in New Mexico [*Magnani et al*., 2004]. Nevertheless, most convergent zones are characterized by wide zones of imbrication and bivergent thrusting associated with the suturing, and the imaged crustal welt in southern Colorado is interpreted to be part of this collision. Notable is the close correlation between this structure and the boundary between the 2.0–1.8 Ga and 1.8–1.7 Ga crustal provinces inferred from, albeit sparse, neodymium isotopic data [*Bennett and DePaolo*, 1987] and the good agreement between the westward continuation of this lineament and the location of this boundary in the Colorado Plateau determined from receiver function analysis [*Gilbert et al*., 2007]. These findings indicate that present Moho depths record the Proterozoic accretional assembly of this region and emphasize the importance of foundational inherited structures in lithospheric architecture [*Dueker et al*., 2001; *Gilbert et al*., 2007; *Karlstrom et al*., 2005; *Karlstrom and Humphreys*, 1998].

6.3. Oligocene Volcanic Flare-Up

[39] The region of lowest crustal shear wave velocities (Figure 6a) is spatially coincident with centers of Oligocene volcanism, especially the San Juan Mountains [*Lipman*, 2007]. The total volcanic output in Colorado during this period is approximately 60,000 km^3, predominantly from the San Juan volcanic field, and the volume of intruded rock is estimated to be on the order of 300,000 km^3 [*Farmer et al*., 2008; *Lipman*, 2007; *Roy et al*., 2004]. Based on their extrusive products, these intrusive bodies likely ranged in composition from andesite to granodiorite [*Lipman*, 2007], which have reduced shear wave velocity (3.1–3.6 km/s) and density (2.62–2.67 g/cm^3) values [*Christensen and Mooney*, 1995; *Christensen*, 1996] relative to the average crustal properties of the adjacent regions (Figure 6a). If the lateral extent of these bodies is approximated by the 2.78 g/cm^3 mean crustal density contour (Figure 6a), then 9 km, or about 20%, of the crust would consist of intrusive rock. This is consistent with the estimated thickness of upper crustal batholiths beneath the San Juan Mountains inferred from gravity and seismic refraction data [*Drenth et al*., 2012; *Roy et al*., 2004]. Therefore, the reduced velocities and densities observed in the western CRM are consistent with Oligocene plutonism.

[40] Despite the voluminous ~300,000 km^3 input of mantle-derived basalts [*Farmer et al*., 2008], it is surprising that the region affected by Oligocene volcanism has some of the thinnest observed crust (Figure 4g). The fate of the mafic residual associated with magmatic differentiation in the Oligocene remains an open question [*Lipman*, 2007], and there is no evidence in the surface wave tomogram for a high-velocity mafic root in the crust beneath the San Juan Mountains (Figure 10). It is possible that the intruded basalts differentiated in the lowermost crust now reside beneath the seismic Moho [*Annen et al*., 2006; *Hildreth and Moorbath*, 1988; *Johnson*, 1991]. Alternatively, dense negatively buoyant restite may have been removed by foundering [*Jull and Kelemen*, 2001; *Kay and Kay*, 1991; *Karlstrom et al*., 2012], as has been suggested for the Sierra Nevada batholith [e.g., *Ducea*, 2002]. Global positioning system data indicate that this entire region is currently in extension, presumably due to the Rio Grande rift system [*Berglund et al*., 2012]; however, any relationship between regions of thin crust and rifting remains ambiguous, and it seems unlikely that the minor amount of extension experienced by the CRM is responsible for the observed variations in Moho depth.

6.4. Mantle Temperature

[41] Lateral shear wave velocity variations up to 0.5 km/s are observed in the upper mantle beneath this region (Figure 7) that are difficult to explain by compositional differences alone, given that velocity modeling of measured mantle mineral properties demonstrates that composition has little effect on shallow mantle velocities [*Cammarano et al*., 2003; *Schutt and Lesher*, 2006]. These results agree with self-consistent thermodynamic modeling indicates that the anharmonic shear wave velocities of pyrolite, peridotite, and pyroxenite only differ by about 0.1 km/s at in situ conditions [*Stixrude and Lithgow-Bertelloni*, 2005]. Therefore, temperature-induced anelastic effects and/or the presence of partial melt are required to explain the range of observed upper mantle velocities [*Stixrude and Lithgow-Bertelloni*, 2005]. Modeling of the effect of partial melt on seismic velocity is conflicted in the literature due to complications arising from the effects of melt distribution geometry and other issues. For example, an ~2.5% shear wave velocity decrement per 1% melt volume is commonly reported [*Hier-Majumder and Courtier*,

2011; *Kreutzmann et al*., 2004; *Takei*, 2000] while *Hammond and Humphreys* [2000] found velocity reductions in excess of 7.9% per 1% melt. The effect of melt on seismic attenuation is also unclear [*Faul et al*., 2004; *Gribb and Cooper*, 2000]. Surface and body-wave tomography results suggest that most of the upper mantle velocity variation in the western United States, including the CRM, can be largely attributed to temperature differences [*Goes and van der Lee*, 2002; *Schmandt and Humphreys*, 2010]. These results, and the lack of consensus on partial melt effects, provide initial justification for modeling mantle velocities via olivine thermal anelasticity. For the purpose of thermal modeling, the mantle is approximated as pure olivine as few constraints exist on the anelastic properties of pyroxene and garnet.

[42] Grain size is a controlling parameter in the *Jackson and Faul* [2010] olivine model used here to map shear velocity to temperature (Figure 7). Both the range and mean of modeled temperatures scale with the assumed grain size. The 1 mm grain size assumed here is consistent with 10 ka peridotite xenoliths erupted from the Rio Grande Rift at Kilbourne Hole in southern New Mexico, which have mean grain sizes of 0.49–1.20 mm [*Satsukawa et al*., 2011]. With the exception of Precambrian diatremes erupted along the Front Range block [*Lester and Farmer*, 1998], there are no reported mantle xenoliths within the CRM. Mantle xenoliths were erupted at the Navajo Volcanic Field (Figure 1), but the wide array of grain sizes (up to several cm) [*Ehrenberg*, 1982], the exotic lithologies [*Smith*, 2010], and the 28–19 Ma eruption age [*Laughlin et al*., 1986] make it difficult to constrain the average olivine grain size beneath the CRM from this xenolith suite.

[43] At 100 km depth, grain sizes of 0.1 mm, 1 mm, and 1 cm result in velocity temperature derivatives (dV_s/dT) of −0.097, −0.077, and −0.065 km/s per 100°C and peak lateral temperature variations of 540°C, 600°C, and 680°C. The resulting mantle densities are thus a function of assumed grain size; however, flexure and gravity modeling results are insensitive to grain size, and similar fits are obtained to observed topography and Bouguer gravity. Only the relative densities are important for these models, and maximum lateral temperature variations for grain sizes ranging 0.1 mm and 1 cm differ by about 140°C, which results in density perturbations of ∼0.5%. A grain size of 1 cm is untenable, however, as this value results in unrealistic temperatures that locally exceed 1500°C at 123 km depth.

[44] Thermal modeling demonstrates that the range of observed mantle shear wave velocities can be attributed to lateral temperature variations of up to ∼600°C, but we note that these results do not exclude the presence of partial melt. Velocities below 4.2–4.3 km/s are observed in the surface wave tomogram (Figure 7), and *Rau and Forsyth* [2011] have argued that such velocities are indicative of melt. If melt is present, the modeled temperature variation is an upper bound, since the velocity-reducing effects of melt porosity have not been taken into account. The *Jackson and Faul* [2010] model naturally predicts seismic attenuation values, and further study focusing on the attenuation structure of the CRM mantle would provide a direct test of our temperature model and could constrain potential melt porosity [e.g., *Yang et al*., 2007].

6.5. S_p Imaging

[45] Negative polarity S_p conversions from the upper mantle are commonly interpreted as the LAB [e.g., *Rychert et al*., 2005], although in regions of thick cratonic lithosphere, many of these arrivals are clearly internal to the lithosphere and an LAB arrival is generally not observed [*Abt et al*., 2010; *Fischer et al*., 2010; *Rychert et al*., 2010]. The CRM region occupies the lithospheric transition from North American craton to the thinner western United States [*Yuan et al*., 2011], which must be taken into consideration when interpreting the *S* wave receiver function results (Figure 8). Our best evidence for an LAB arrival is found beneath the Colorado Plateau, where negative arrivals at 100–150 km depth (Figure 8) are coincidentally imaged with a rapid increase in the inferred temperature field (Figure 7). This result and interpretation are consistent with several previous studies, including analyses of *S* wave receiver function data from the TA [*Kumar et al*., 2012; *Levander and Miller*, 2012], surface wave inversion from the Colorado Plateau/Rio Grande Rift Seismic Transect Experiment (LA RISTRA) [*West et al*., 2004], the joint inversion of regional seismic and gravity data [*Bailey et al*., 2012], and magnetotelluric results from a transect across the western Plateau [*Wannamaker et al*., 2008].

[46] The deepest negative polarity arrivals are observed beneath the High Plains and extend westward beneath much of the CRM, indicating that the lithosphere is at least 150–200 km thick in this region. This is consistent with our surface wave modeling, which finds persistent high velocities and cool temperatures at shallower depths in the

Front Range and High Plains mantle (Figure 7). A negative velocity gradient is not observed in the tomogram at these depths, but surface wave model depth resolution is poor below 120 km depth. Body-wave tomography from CREST and TA data show that the fast upper mantle beneath the High Plains terminates near 200 km depth [*Schmandt and Humphreys*, 2010; *MacCarthy*, 2011], consistent with the interpretation of this deep negative arrival as the LAB.

[47] This finding conflicts with previous *S* wave receiver function studies that interpret lithospheric thicknesses of less than 120 km for the Colorado High Plains [*Kumar et al*., 2012; *Levander and Miller*, 2012]. We propose that the shallower secondary negative arrival imaged above 100 km depth in this region (Figures 8a–8c) and differing methodologies have obscured the deeper LAB arrival in these other studies. Additionally, our preliminary *S* wave receiver function analysis of TA data [*Foster et al*., 2012] shows that this deep negative velocity gradient at 150–200 km depth extends further east into the Great Plains, consistent with thick cratonic lithosphere in this region estimated from anisotropic surface wave tomography [*Yuan et al*., 2011]. These results suggest a step in lithospheric thickness across the CRM, with thickness increasing by approximately 50 km from the Colorado Plateau to the High Plains.

[48] The broad negative arrival imaged beneath the CRM above 100 km depth is an intriguing feature that has been previously interpreted as the LAB [*Abt et al*., 2010; *Kumar et al*., 2012; *Levander and Miller*, 2012]. However, the results from this study cast doubt on this explanation, and we speculate that this arrival may be internal to the lithosphere. There is still a debate on the origin of the seismic LAB [*Fischer et al*., 2010], but if it is related to the thermal boundary layer, then presumably the CRM LAB should be between 120 and 170 km deep based on the observation that the mean CRM geotherm sits between that of the Colorado Plateau and High Plains in terms of absolute temperature and thermal gradient between 98 and 123 km depth (Figure 7d). Additionally, the shallow S_p arrival extends eastward and overlaps with the deeper LAB arrival and elevated upper mantle seismic velocities observed beneath the Front Range-High Plains region (Figures 8b–8c east of −107°).

[49] If this arrival was the LAB, then the CRM lithosphere would be of similar thickness to that of the southern margin of the Colorado Plateau [*Kumar et al*., 2012; *Levander and Miller*, 2012]. However, the analysis of Neogene volcanism indicates that CRM basalts were primarily derived from a lithospheric source [*Beard and Johnson*, 1997] while the southern Plateau has been more strongly modified by asthenospheric melts [*Crow et al*., 2011], which implies a thicker CRM lithosphere. Additionally, we note that both the Precambrian diamondiferous diatremes in the Front Range [*Lester and Farmer*, 1998; *McCallum et al*., 1979] and xenoliths from 140 km depth erupted in the Navajo Volcanic Field (28–19 Ma) [*Riter and Smith*, 1996] indicate the presence of thick lithosphere in the past and it remains unclear, given the lack of major extension in the CRM, what mechanisms would be responsible for thinning the lithosphere.

[50] Shallow sub-Moho negative arrivals are also observed in the *P* wave receiver function image (Figure 4), although these arrivals are not as prominent or laterally continuous as in the *S* wave image. This discrepancy may be due to frequency-dependent effects resulting from heterogeneous velocities in this region. The images become more consistent when the *P* wave receiver functions are filtered at 3–20 s period and stacked with the same bin sharing as in the *S* wave image (Figure 11); however, in this period range, the shallow negatives begin to interfere with the Moho side lobe, and additional modeling will be required to investigate the detailed velocity structure in this depth region. The deep LAB arrival beneath the High Plains is not observed in the *P* wave images but crustal reverberations interfere with arrivals from this interval (Figure 11).

[51] The interpretation of this intralithospheric feature is difficult because there is no consensus regarding the origin of negative S_p conversions from within the mantle lithosphere. Potential mechanisms include a rapid temperature increase [*Rychert et al*., 2010], a change in seismic anisotropy [*Fischer et al*., 2010; *Yuan et al*., 2011], a low-velocity metasomatic layer [*Chen et al*., 2009; *Griffin et al*., 2009; *Wölbern et al*., 2012], and variations in water content [*Karato*, 2012]. Regardless of this ambiguity, the shallow negative energy is spatially correlated with the thermally perturbed lithosphere observed beneath the CRM (Figure 7a) and suggests that these features may be related.

6.6. Cenozoic Volcanism

[52] The region of elevated temperatures in the shallow mantle beneath the CRM is bounded by

occurrences of ultrapotassic rocks, e.g., minettes and lamproites (Figures 1 and 7a), which are thought to arise from partial melting of low-solidus metasomatized mantle lithosphere [*Foley*, 1992; *McKenzie*, 1989]. Most of these rocks were emplaced between 33 and 20 Ma, spanning the Oligocene flare-up and initial extension of the Rio Grande rift system [*Gibson et al*., 1993]. These areas include the Navajo Volcanic Field [*Laughlin et al*., 1986], the Dulce area [*Aldrich et al*., 1986], the Spanish Peaks [*Penn and Lindsey*, 2009], and the Middle Park lamproite [*Thompson et al*., 1997] (Figure 1). An additional period of ultrapotassic volcanism occurred in northwest Colorado at 10–8 Ma [*Leat et al*., 1991; *Thompson et al*., 1990] during a renewed period of rift activity [*Aldrich et al*., 1986; *Ingersoll*, 2001; *Landman and Flowers*, 2013]. Therefore, thermal modification of the mantle lithosphere probably began in the Oligocene and likely continued until at least the end of the Miocene.

[53] Despite being primarily lithospheric in origin [*Beard and Johnson*, 1997], the composition of late Cenozoic basalts in Colorado indicate some mixing with melts derived from the underlying asthenosphere [*Crow et al*., 2011; *Leat et al*., 1990]. Of particular note are Quaternary basalts erupted in northwest Colorado that record mixing with minette composition magmas [*Leat et al*., 1989]. Therefore, we suggest that the elevated temperatures observed in the CRM mantle are the result of heat advected into the lithosphere by melt infiltration from the underlying mantle. The shallow negative velocity gradient imaged beneath the CRM could represent melt stagnated within the lithosphere, as has been proposed for the Tanzanian Craton at the East African Rift [*Wölbern et al*., 2012]. It is difficult to speculate on the origin of the sublithospheric melt, but we note that body-wave tomography shows that reduced mantle velocities extend to the mantle transition zone beneath the CRM [*Schmandt and Humphreys*, 2010; *MacCarthy*, 2011].

7. Conclusions

[54] The CREST-seismic results show that the lithosphere of the CRMs exhibits marked contrast to the adjacent High Plains and Colorado Plateau provinces. Despite Laramide shortening and magmatic addition since the Oligocene, receiver function imaging indicates that the CRM crust is thinner with respect to adjacent regions. Thickened crust is observed near the Cheyenne belt and the Yavapai-Mazatzal boundary, indicating that ancient structures, left from the assembly of North America, remain an important control on modern lithospheric architecture. The highest topography clearly lacks a crustal root, which refutes a model of Airy-Heiskanen isostasy in this region. Reduced shear wave velocities suggest that the Colorado Rockies are compensated by both Pratt-Hayford density variations within the crust and by density variations in the upper mantle. This conclusion is supported by density and flexure modeling results that predict the long-wavelength topography and a peak differential elevation of 1.7 km between the Rockies and the surrounding provinces.

[55] Buoyancy-generating structures are attributed to the Cenozoic history of this region. Lowest velocity and density values in the crust are observed beneath centers of Oligocene volcanism, the San Juan Mountains in particular, and are interpreted as due to the emplacement of large plutonic complex associated with the ignimbrite flare-up. Surface wave tomography demonstrates that the mantle beneath the Rockies is heterogeneous and modeling suggests that lateral thermal variations reach ~600°C (the potential of partial melt makes this an upper bound). *S* wave receiver function imaging indicates that the LAB increases in depth by 50 km from the Colorado Plateau to the High Plains and the shallow negative polarity arrivals observed beneath the Rockies (above 100 km depth) are interpreted as internal to the lithosphere. These observations are attributed to heating and partial melting of the mantle during the Cenozoic as evidenced by volcanic rocks and suggest the ongoing internal modification of once-stable mantle lithosphere.

Appendix : A

A1. Flexure and Gravity

A.1.1. Flexure Modeling

[56] Surface topography is predicted from the density model $\rho_{\mathrm{obs}}(\mathbf{x}, z)$, which includes crustal thickness variations and crust and upper mantle lateral density differences. The net vertical load acting on the lithosphere is a combination of subsurface buoyancy forces and the mantle-restoring forces resulting from flexure. To maintain static equilibrium, the difference between these forces is accommodated by elastic flexure. The net downward directed load $\boldsymbol{l}(\mathbf{x})$ on the flexed plate can be written as

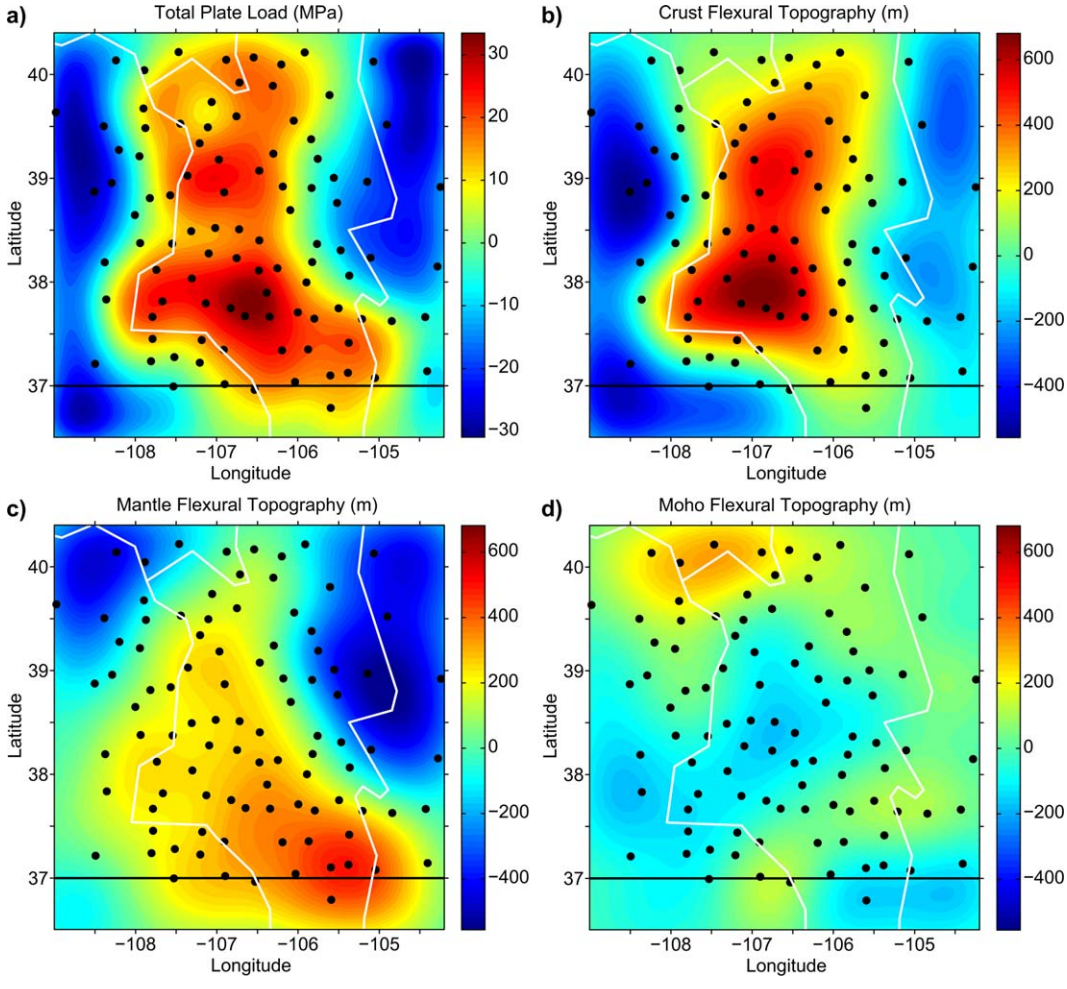

Figure A1. Buoyancy contributions to net plate flexure. (a) The total plate load derived from the modeled densities. (b) The component of plate flexure (Figure 9) resulting from crustal density variations. (c) Flexure due to mantle density variations. (d) Flexure due to the Moho depth variations.

$$\boldsymbol{l}(\mathbf{x}) = \rho_a \boldsymbol{g} \boldsymbol{w}(\mathbf{x}) + \int_{z_1}^{z_2} [\rho_{\mathrm{mod}}(\mathbf{x}, z) - \rho_{\mathrm{ref}}(z)] \boldsymbol{g}(z) \mathrm{d}z, \quad \text{(A1)}$$

where the term $\rho_a \boldsymbol{g}$ is the pressure gradient in the asthenosphere and represents the mantle-restoring force, $\boldsymbol{w}(\mathbf{x})$ is the vertical displacement due to plate flexure, the vertical integration bounds encompass the density model from the surface at $z_1 = 0$ km to $z_2 = 170$ km depth, $\boldsymbol{g}(z)$ is acceleration due to gravity as a function of depth and $\rho_{\mathrm{ref}}(z)$ is a reference density column in isostatic equilibrium. The density of the asthenosphere ρ_a is assumed to be 3.36 g/cm^3, and density values from the preliminary reference Earth model (PREM) reference model are used to calculate $\boldsymbol{g}(z)$ [*Dziewonski and Anderson*, 1981]. The subsurface buoyancy load represented by the integral in equation is not a function of plate flexure because the density structure is estimated from in situ seismic velocities, which already include the (unknown) effects of plate flexure. The total buoyancy load and the contributions from the crust, Moho and mantle depths for the CREST array are shown in Figure A1.

[57] The bending of an isotropic homogeneous plate in response to a distributed load $\boldsymbol{l}(\mathbf{x})$ is given by the biharmonic equation

$$\boldsymbol{D}\nabla^2\nabla^2\boldsymbol{w}(\mathbf{x}) = -\boldsymbol{l}(\mathbf{x}) \text{ and } \boldsymbol{D} = \frac{\boldsymbol{T}_e{}^3 \boldsymbol{E}}{12(1-\nu^2)}, \quad \text{(A2)}$$

where ∇^2 is the Laplacian, $\boldsymbol{D}$ is the flexural rigidity, $\boldsymbol{T}_e$ is the elastic thickness, $\boldsymbol{E}$ is Young's modulus which is assumed to be 10^{11} Pa, and ν is Poisson's ratio which is assumed to be 0.25. Taking the two-dimensional Fourier transform of $\boldsymbol{w}$ and $\boldsymbol{l}$ in equation (A2) yields

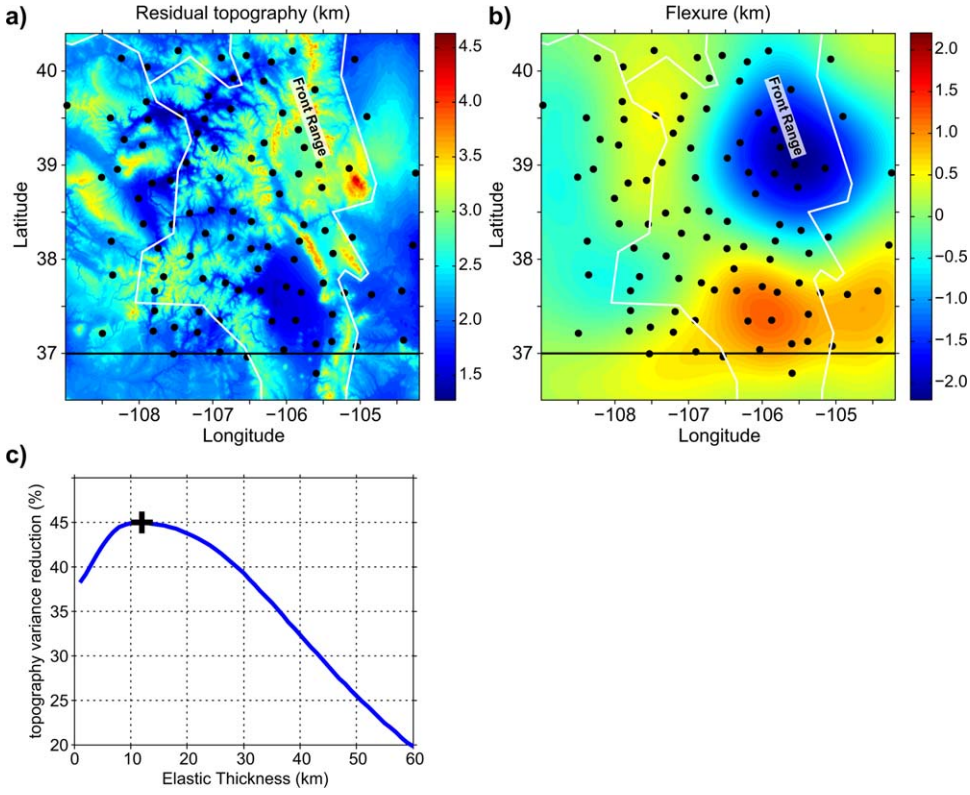

Figure A2. Residual topography and elastic thickness estimation. (a) Elevation misfit between the flexure model (Figure 9) and observed topography. (b) Plate flexure due to a surface load derived from the residual topography in Figure A2a. (c) Assumed elastic thickness is plotted against topographic variance reduction. Flexure modeling is performed for each thickness value using the load in Figure A2a and the best fit elastic thickness (12 km) is plotted as a "+" symbol.

$$\boldsymbol{D}\left(\boldsymbol{k}_x^4 + \boldsymbol{k}_y^4 + 2\boldsymbol{k}_x^2\boldsymbol{k}_y^2\right)\boldsymbol{W}(\mathbf{k}) = -\boldsymbol{L}(\mathbf{k}), \tag{A3}$$

where $\boldsymbol{k}_x, \boldsymbol{k}_y$ are the horizontal components of the two-dimensional wavenumber vector $\mathbf{k}$. $\boldsymbol{L}(\mathbf{k})$ is obtained by transforming the plate load in equation which yields

$$\begin{aligned} &\boldsymbol{L}(\mathbf{k}) = \rho_a \boldsymbol{g}\boldsymbol{W}(\mathbf{k}) + \boldsymbol{Q}(\mathbf{k}), \text{ where} \\ &\boldsymbol{Q}(\mathbf{k}) = \mathscr{F}^2\left\{\int_{z_1}^{z_2} \rho_{\text{mod}}(\mathbf{x}, z)\boldsymbol{g}(z)dz\right\}(\mathbf{k}) + C, \end{aligned} \tag{A4}$$

where $\mathscr{F}^2\{\cdot\}$ denotes the two-dimensional Fourier transform and C is a constant which depends on the reference density column $\rho_{ref}(z)$. In practice, we are interested only in the relative deflections, which do not depend on the assumed reference column, and thus $\boldsymbol{Q}$ is calculated by evaluating the integral in (A4), removing the mean and then applying the fast Fourier transform. A zero mean also helps to reduce edge effects associated with the filtering process and wrapping effects are avoided via zero padding the plate load in the spatial domain by the flexural wavelength.

[59] Finally, plate flexure can be calculated using

$$\boldsymbol{W}(\mathbf{k}) = \frac{-\boldsymbol{Q}(\mathbf{k})}{\boldsymbol{D}\left(\boldsymbol{k}_x^4 + \boldsymbol{k}_y^4 + 2\boldsymbol{k}_x^2\boldsymbol{k}_y^2\right) + \rho_a \boldsymbol{g}}, \tag{A5}$$

and taking the inverse Fourier transform to get $\boldsymbol{w}(\mathbf{x})$. The elastic thickness is determined empirically by maximizing the variance reduction of the observed topography (Figure A2c). The resulting misfit between the actual and observed topography (Figure A2a) can then used to test the validity of the best-fit elastic thickness and the modeling assumptions by applying the residual topography as a surface load and modeling the resulting plate flexure (Figure A2b).

A.1.2. Gravity Modeling

[60] Bouguer gravity is predicted from the density model $\rho_{\text{obs}}(\mathbf{x}, z)$ at a fixed surface location by

calculating the vertical gravitation due to each model block with the analytic solution for a rectangular prism [*Nagy et al.*, 2000]:

$$g_z = G\rho_{\mathrm{obs}}(\mathbf{x},z)\left|\left|\left| x\ln(y+r)+y\ln(x+r) - z\tan^{-1}\frac{xy}{zr}\right|_{x_1}^{x_2}\right|_{y_1}^{y_2}\right|_{z_1}^{z_2} \quad \text{(A6)}$$

where $\mathbf{x} = [x \quad y]$ is the horizontal position vector of the model block relative to the observation location where g_z is measured, G is the gravitational constant, and $r=\sqrt{x^2+y^2+z^2}$ is the block distance. Numeric volume integration is then performed to obtain total gravitation. The top of the density model is flat and is set to the minimum station elevation, which therefore approximates the Bouguer gravity field.

Acknowledgments

[61] We thank Weisen Shen and Mike Ritzwoller for providing the long period Raleigh wave phase velocity measurements. Uli Faul provided the MATLAB scripts used to calculate olivine anelasticity. We also thank the CREST working group. Tony Lowry and an anonymous reviewer provided valuable comments on this manuscript. The instruments used in the field deployment were provided by the Incorporated Research Institutions for Seismology (IRIS) via the PASSCAL Instrument Center at New Mexico Tech. Data collected during this experiment are available through the IRIS Data Management Center. The facilities of the IRIS Consortium are supported by the National Science Foundation under cooperative agreement EAR-0552316 and by the Department of Energy National Nuclear Security Administration. The CREST experiment was supported by grants EAR-0607693, 0607837, and 0607808 from the NSF Continental Dynamics Program.

References

Abt, D. L., K. M. Fischer, S. W. French, H. A. Ford, H. Yuan, and B. Romanowicz (2010), North American lithospheric discontinuity structure imaged by Ps and Sp receiver functions, *J. Geophys. Res.*, *115*, B09301, doi:10.1029/2009JB006914.

Afonso, J. C., G. Ranalli, and M. Fernandez (2005), Thermal expansivity and elastic properties of the lithospheric mantle: Results from mineral physics of composites, *Phys. Earth Planet. Inter.*, *149*(3), 279–306, doi:10.1016/j.pepi.2004.10.003.

Aki, K. (1957), Space and time spectra of stationary stochastic waves with special reference to microtremors, *Bull. Earthquake Res. Inst.*, *35*, 415–456.

Aldrich M. J. Jr., C. E. Chapin, A. W. Laughlin, and G. R. Keller (1986), Stress history and tectonic development of the Rio Grande Rift, New Mexico, *J. Geophys. Res.*, *91*, 6199–6211.

Annen, C., J. D. Blundy, and R. S. Sparks (2006), The genesis of intermediate and silica magmas in Deep Crustal Hot Zones, *J. Petrol.*, *47*(3), 505–539.

Aster, R. C., B. Borchers, and C. H. Thurber (2012), *Parameter Estimation and Inverse Problems*, 2nd ed., Academic Press, Waltham, Mass.

Baig, A. M., M. G. Bostock, and J.-P. Mercier (2005), Spectral reconstruction of teleseismic P Green's functions, *J. Geophys. Res.*, *110*, B08306, doi:10.1029/2005JB003625.

Bailey, I. W., M. S. Miller, K. Liu, and A. Levander (2012), Vs and density structure beneath the Colorado Plateau constrained by gravity anomalies and joint inversions of receiver function and phase velocity data, *J. Geophys. Res.*, *117*, B02313, doi:10.1029/2011JB008522.

Baldridge, W. S., G. R. Keller, V. Haak, E. Wendlandt, G. R. Jiracek, and K. H. Olsen (1995), *The Rio Grande Rift, in Developments in Geotectonics, vol. 25*, edited by K. H. Olsen, pp. 233–275, Elsevier, Amsterdam, doi:10.1016/S0419-0254(06)80014-5.

Beard, B. L., and C. M. Johnson (1997), Hafnium isotope evidence for the origin of Cenozoic basaltic lavas from the Southwestern United States, *J. Geophys. Res.*, *102*, 20,149–120,178, doi:10.1029/97JB01731.

Bechtel, T. D., D. W. Forsyth, V. L. Sharpton, and R. A. F. Grieve (1990), Variations in effective elastic thickness of the North American lithosphere, *Nature*, *343*(6259), 636–638.

Becker, T. W. (2012), On recent seismic tomography for the western United States, *Geochem. Geophys. Geosyst.*, *13*, Q01W10, doi:10.1029/2011GC003977.

Bennett, V. C., and D. DePaolo, J. (1987), Proterozoic crustal history of the Western United States as determined by neodymium isotopic mapping; with Suppl. Data 87-30, *GSA Bull.*, *99*(5), 674–685, doi:10.1130/0016-7606(1987)99<674:PCHOTW>2.0.CO;2.

Bensen, G. D., M. H. Ritzwoller, M. P. Barmin, A. L. Levshin, F. Lin, M. P. Moschetti, N. M. Shapiro, and Y. Yang (2007), Processing seismic ambient noise data to obtain reliable broad-band surface wave dispersion measurements, *Geophys. J. Int.*, *169*(3), 1239–1260, doi:10.1111/j.1365-246X.2007.03374.x.

Berglund, H. T., A. F. Sheehan, M. H. Murray, M. Roy, A. R. Lowry, R. S. Nerem, and F. Blume (2012), Distributed deformation across the Rio Grande Rift, Great Plains and Colorado Plateau, *Geology*, *40*(1), 23–26, doi:10.1130/G32418.1.

Bostock, M. G. (2004), Green's functions, source signatures, and the normalization of teleseismic wave fields, *J. Geophys. Res.*, *109*, B03303, doi:10.1029/2003JB002783.

Boyd, O. S., and A. F. Sheehan (2005), Attenuation tomography beneath the Rocky Mountain front; implications for the physical state of the upper mantle, in *The Rocky Mountain Region—An Evolving Lithosphere: Tectonics, Geochemistry, and Geophysics, Geophys. Monogr. Ser.*, vol. 154, edited by K. E. Kalstrom and G. R. Keller, pp. 361–377, AGU, Washington, D. C., doi:10.1029/154GM27.

Brister, B. S., and R. R. Gries (1994), Tertiary stratigraphy and tectonic development of the Alamosa Basin (northern San Luis Basin), Rio Grande Rift, south-central Colorado, *Geol. Soc. Am. Spec.* Paper, *291*, 39–58.

Brocher, T. A. (2005), Empirical relations between elastic wavespeeds and density in the earth's crust, *Bull. Seismol. Soc. Am.*, *95*(6), 2081–2092, doi:10.1785/0120050077.

Burov, E. B., and M. Diament (1995), The effective elastic thickness (Te) of continental lithosphere: What does it really

mean?, *J. Geophys. Res.*, *100*, 3905–3927, doi:10.1029/94JB02770.

Cammarano, F., S. Goes, P. Vacher, and D. Giardini (2003), Inferring upper-mantle temperatures from seismic velocities, *Phys. Earth Planet. Inter.*, *138*(3), 197–222, doi:10.1016/S0031–9201(03)00156-0.

Chamberlain, K. (1998), Medicine Bow Orogeny; timing of deformation and model of crustal structure produced during continent-arc collision, ca. 1.78 Ga, southeastern Wyoming, *Rocky Mountain Geol.*, *33*(2), 259–277, doi:10.2113/33.2.259.

Chapin, C. E. (2012), Origin of the Colorado mineral belt, *Geosphere*, *8*(1), 28–43, doi:10.1130/ges00694.1.

Chapin, C. E., M. Wilks, W. C. McIntosh, S. M. Cather, and S. A. Kelley (2004), Space-time patterns of Late Cretaceous to present magmatism in New Mexico; comparison with Andean volcanism and potential for future volcanism, *Bull. N. M. Bur. Geol. Miner. Resour. 160*, 13–40.

Chen, C.-W., S. Rondenay, R. L. Evans, and D. B. Snyder (2009), Geophysical detection of relict metasomatism from an Archean (~3.5 Ga) subduction zone, *Science*, *326*(5956), 1089–1091, doi:10.1126/science.1178477.

Christensen, N. I. (1996), Poisson's ratio and crustal seismology, *J. Geophys. Res.*, *101*, 3139–3156, doi:10.1029/95JB03446.

Christensen, N. I., and W. D. Mooney (1995), Seismic velocity structure and composition of the continental crust; a global view, *J. Geophys. Res.*, *100*, 9761–9788, doi:10.1029/95JB00259.

Coblentz, D., C. G. Chase, K. E. Karlstrom, and J. van Wijk (2011), Topography, the geoid, and compensation mechanisms for the southern Rocky Mountains, *Geochem. Geophys. Geosyst.*, *12*, Q04002, doi:10.1029/2010gc003459.

Coney, P. J., and S. J. Reynolds (1977), Cordilleran Benioff zones, *Nature*, *270*, 403–406, doi:10.1038/270403a0.

Crosswhite, J. A., and E. D. Humphreys (2003), Imaging the mountainless root of the 1.8 Ga Cheyenne belt suture and clues to its tectonic stability, *Geology*, *31*(8), 669–672, doi:10.1130/G19552.1.

Crow, R., K. Karlstrom, Y. Asmerom, B. Schmandt, V. Polyak, and S. A. DuFrane (2011), Shrinking of the Colorado Plateau via lithospheric mantle erosion: Evidence from Nd and Sr isotopes and geochronology of Neogene basalts, *Geology*, *39*(1), 27–30, doi:10.1130/g31611.1.

Decker, E. R. (1995), Thermal regimes of the Southern Rocky Mountains and Wyoming Basin in Colorado and Wyoming in the United States, *Tectonophysics*, *244*(1), 85–106, doi:10.1016/0040–1951(94)00219-Y.

Drenth, B. J., G. R. Keller, and R. A. Thompson (2012), Geophysical study of the San Juan Mountains batholith complex, southwestern Colorado, *Geosphere*, *8*(3), 669–684, doi:10.1130/ges00723.1.

Ducea, M. N. (2002), Constraints on the bulk composition and root foundering rates of continental arcs: A California arc perspective, *J. Geophys. Res.*, *107*(B11), 2304, doi:10.1029/2001jb000643.

Dueker, K. G., and A. F. Sheehan (1997), Mantle discontinuity structure from midpoint stacks of converted P and S waves across the Yellowstone hotspot track, *J. Geophys. Res.*, *102*, 8313–8327, doi:10.1029/96JB03857.

Dueker, K., H. Yuan, and B. Zurek (2001), Thick-structured Proterozoic lithosphere of the Rocky Mountain region, *GSA Today*, *11*(12), 4–9.

Dziewonski, A. M., and D. L. Anderson (1981), Preliminary reference Earth model, *Phys. Earth Planet. Inter.*, *25*(4), 297–356, doi:10.1016/0031–9201(81)90046-7.

Eaton, G. P. (2008), Epeirogeny in the Southern Rocky Mountains region: Evidence and origin, *Geosphere*, *4*(5), 408–408, doi:10.1130/ges00149.1.

Ehrenberg, S. N. (1982), Petrogenesis of garnet lherzolite and megacrystalline nodules from the Thumb, Navajo volcanic field, *J. Petrol.*, *23*(4), 507–547, doi:10.1093/petrology/23.4.507.

Ekström, G., G. A. Abers, and S. C. Webb (2009), Determination of surface-wave phase velocities across US Array from noise and Aki's spectral formulation, *Geophys. Res. Lett.*, *36*, L18301, doi:10.1029/2009GL039131.

Erslev, E. A. (1993), Thrusts, back-thrusts, and detachments of Rocky Mountain foreland arches, in *Laramide Basement Deformation in the Rocky Mountain Foreland of the Western United States*, edited by C. J. Schmidt, et al., pp. 339–358, Geol. Soc. of Am. Spec. Paper 280.

Farmer, G. L., T. Bailley, and L. T. Elkins-Tanton (2008), Mantle source volumes and the origin of the mid-Tertiary ignimbrite flare-up in the southern Rocky Mountains, western US, *Lithos*, *102*(1), 279–294, doi:10.1016/j.lithos.2007.08.014.

Faul, U. H., J. D. F. Gerald, and I. Jackson (2004), Shear wave attenuation and dispersion in melt-bearing olivine polycrystals: 2. Microstructural interpretation and seismological implications, *J. Geophys. Res.*, *109*, B06202, doi:10.1029/2003jb002407.

Fischer, K. M., H. A. Ford, D. L. Abt, and C. A. Rychert (2010), The lithosphere-asthenosphere boundary, *Annu. Rev. Earth Planet. Sci.*, *38*, 551–575, doi:10.1146/annurev-earth-040809–152438.

Foley, S. (1992), Vein-plus-wall-rock melting mechanisms in the lithosphere and the origin of potassic alkaline magmas, *Lithos*, *28*(3), 435–453, doi:10.1016/0024-4937(92)90018-T.

Forte, A. M., R. Moucha, N. A. Simmons, S. P. Grand, and J. X. Mitrovica (2010), Deep-mantle contributions to the surface dynamics of the North American continent, *Tectonophysics*, *481*(1), 3–15, doi:10.1016/j.tecto.2009.06.010.

Foster, K., K. Dueker, J. McClenahan, S. M. Hansen, B. Schmandt (2012), A taxonomy of three species of negative velocity arrivals in the lithospheric mantle beneath the United States using Sp receiver functions, paper presented at 2012 Fall Meeting, AGU, San Francisco, Calif.

Gibson, S. A., R. N. Thompson, P. T. Leat, M. A. Morrison, G. L. Hendry, A. P. Dickin, and J. G. Mitchell (1993), Ultrapotassic magmas along the flanks of the Oligo-Miocene Rio Grande Rift, USA: Monitors of the zone of lithospheric mantle extension and thinning beneath a continental rift, *J. Petrol.*, *34*(1), 187–228, doi:10.1093/petrology/34.1.187.

Gilbert, H. (2012), Crustal structure and signatures of recent tectonism as influenced by ancient terranes in the Western United States, *Geosphere*, *8*(1), 141–157, doi:10.1130/GES00720.1.

Gilbert, H. J., and A. F. Sheehan (2004), Images of crustal variations in the intermountain west, *J. Geophys. Res*, *109*, B03306, doi:10.1029/2003JB002730.

Gilbert, H., A. A. Velasco, and G. Zandt (2007), Preservation of Proterozoic terrane boundaries within the Colorado Plateau and implications for its tectonic evolution, *Earth Planet. Sci. Lett.*, *258*, 237–248, doi:10.1016/j.epsl.2007.03.034.

Goes, S., and S. van der Lee (2002), Thermal structure of the North American uppermost mantle inferred from seismic tomography, *J. Geophys. Res*, *107*(B3), 2050, doi:10.1029/2000JB000049.

Gribb, T. T., and R. F. Cooper (2000), The effect of an equilibrated melt phase on the shear creep and attenuation behavior of polycrystalline olivine, *Geophys. Res. Lett.*, *27*, 2341–2344, doi:10.1029/2000gl011443.

Griffin, W. L., S. Y. O'Reilly, J. C. Afonso, and G. C. Begg (2009), The composition and evolution of lithospheric mantle; A re-evaluation and its tectonic implications, *J. Petrol.*, *50*(7), 1185–1204, doi:10.1093/petrology/egn033.

Hager, B. H., and M. A. Richards (1989), Long-wavelength variations in Earth's geoid: Physical models and dynamical implications, *Philos. Trans. R. Soc. A*, *328*, 309–327.

Hammond, W. C., and E. D. Humphreys (2000), Upper mantle seismic wave attenuation: Effects of realistic partial melt distribution, *J. Geophys. Res.*, *105*, 10,987–10,999, doi:10.1029/2000JB900042.

Hansen, S., and K. Dueker (2009), P and S Wave receiver function images of crustal imbrication beneath the Cheyenne Belt in Southeast Wyoming, *Bull. Seismol. Soc. Am.*, *99*(3), 1953–1961, doi:10.1785/0120080168.

Helffrich, G. (2006), Extend-time multitaper frequency domain cross-correlation receiver-function estimation, *Bull. Seismol. Soc. Am.*, *96*(1), 344–347, doi:10.1785/0120050098.

Heller, P. L., K. G. Dueker, and M. E. McMillan (2003), Post-Paleozoic alluvial gravel transport as evidence of continental tilting in the U.S. Cordillera, *GSA Bull.*, *115*(9), 1122–1132, doi:10.1130/B25219.1.

Herrmann, R. B., and C. J. Ammon (2002), *Computer Programs in Seismology*, Saint Louis Univ., Mo.

Hildreth, W., and S. Moorbath (1988), Crustal contributions to arc magmatism in the Andes of central Chile, *Contrib. Mineral. Petrol.*, *98*(4), 455–489, doi:10.1007/BF00372365.

Hirschmann, M. M. (2000), Mantle solidus: Experimental constraints and the effects of peridotite composition, *Geochem. Geophys. Geosyst.*, *1*, 1042, doi:10.1029/2000GC000070.

Hier-Majumder, S., and A. Courtier (2011), Seismic signature of small melt fraction atop the transition zone, *Earth Planet. Sci. Lett.*, *308*(3), 334–342, doi:10.1016/j.epsl.2011.05.055.

Humphreys, E., E. Hessler, K. Dueker, G. L. Farmer, E. Erslev, and T. Atwater (2003), How laramide-age hydration of North American Lithosphere by the Farallon Slab controlled subsequent activity in the Western United States, *Int. Geol. Rev.*, *45*(7), 575–595, doi:10.2747/0020–6814.45.7.575.

Ingersoll, R. V. (2001), Structural and stratigraphic evolution of the Rio Grande Rift, northern New Mexico and southern Colorado, *Int. Geol. Rev.*, *43*(10), 867–891, doi:10.1080/00206810109465053.

Jackson, I., and U. H. Faul (2010), Grainsize-sensitive viscoelastic relaxation in olivine: Towards a robust laboratory--based model for seismological application, *Phys. Earth Planet. Inter.*, *183*(1), 151–163, doi:10.1016/j.pepi.2010.09.005.

Johnson, C. M. (1991), Large-scale crust formation and lithosphere modification beneath middle to late Cenozoic calderas and volcanic fields, western North America, *J. Geophys. Res.*, *96*, 13,485–13,507, doi:10.1029/91JB00304.

Jones, C. H., G. L. Farmer, B. Sageman, and S. Zhong (2011), Hydrodynamic mechanism for the Laramide orogeny, *Geosphere*, *7*(1), 183–201, doi:10.1130/GES00575.1.

Jull, M., and P. B. Kelemen (2001), On the conditions for lower crustal convective instability, *J. Geophys. Res.*, *106*, 6423–6446, doi:10.1029/2000JB900357.

Karato, S. (1993), Importance of anelasticity in the interpretation of seismic tomography, *Geophys. Res. Lett.*, *20*, 1623–1626, doi:10.1029/93GL01767.

Karato, S.-I. (2012), On the origin of the asthenosphere, *Earth Planet. Sci. Lett.*, *321*, 95–103, doi:10.1016/j.epsl.2012.01.001.

Karlstrom, K. E., and R. S. Houston (1984), The Cheyenne belt: Analysis of a Proterozoic suture in southern Wyoming, *Precambrian Res.*, *25*, 415–446, doi:10.1016/0301-9268(84)90012-3.

Karlstrom, K., E., and E. Humphreys, D. (1998), Persistent influence of Proterozoic accretionary boundaries in the tectonic evolution of southwestern North America; interaction of cratonic grain and mantle modification events, *Rocky Mountain Geol.*, *33*, 161–179, doi:10.2113/33.2.161.

Karlstrom, K. E., S. J. Whitmeyer, K. Dueker, M. L. Williams, S. A. Bowring, A. R. Levander, E. D. Humphreys, and G. R. Keller (2005), Synthesis of results from the CD-ROM Experiment: 4-D image of the lithosphere beneath the Rocky Mountains and implications for understanding the evolution of continental lithosphere, in *The Rocky Mountain Region—An Evolving Lithosphere: Tectonics, Geochemistry, and Geophysics, Geophys. Monogr. Ser.*, vol. 154, edited by K. E. Kalstrom and G. R. Keller, pp. 421–441, AGU, Washington, D. C., doi:10.1029/154GM31.

Karlstrom, K. E., et al. (2012), Mantle-driven dynamic uplift of the Rocky Mountains and Colorado Plateau and its surface response: Toward a unified hypothesis, *Lithosphere*, *4*(1), 3–22, doi:10.1130/L150.1.

Kay, R. W., and S. M. Kay (1991), Creation and destruction of lower continental crust, *Geol. Rundsch.*, *80*(2), 259–278, doi:10.1007/BF01829365.

Keller, G. R., M. A. Khan, P. Morgan, R. F. Wendlandt, W. S. Baldridge, K. H. Olsen, C. Prodehl, and L. W. Braile (1991), A comparative study of the Rio Grande and Kenya rifts, *Tectonophysics*, *197*(2), 355–371, doi:10.1016/0040-1951(91)90050-3.

Keller, G. R., et al. (2006), A community effort to construct a gravity database for the United States and an associated Web portal, *Geol. Soc. Am. Spec. Paper*, *397*, 21–34.

Kennett, B. L. N., E. R. Engdahl, and R. Buland (1995), Constraints on seismic velocities in the Earth from traveltimes, *Geophys. J. Int.*, *122*(1), 108–124, doi:10.1111/j.1365-246X.1995.tb03540.x.

Kind, R., X. Yuan, and P. Kumar (2012), Seismic receiver functions and the lithosphere-asthenosphere boundary, *Tectonophysics*, *536–537*, 25–43, doi:10.1016/j.tecto.2012.03.005.

Kluth, C. F., and P. J. Coney (1981), Plate-tectonics of the Ancestral Rocky Mountains, *Geology*, *9*(1), 10–15, doi:10.1130/0091–7613(1981)9<10:ptotar>2.0.co;2.

Kreutzmann, A., H. Schmeling, A. Junge, T. Ruedas, G. Marquart, and I. T. Bjarnason (2004), Temperature and melting of a ridge-centred plume with application to Iceland. Part II. Predictions for electromagnetic and seismic observables, *Geophys. J. Int.*, *159*(3), 1097–1111, doi:10.1111/j.1365-246X.2004.02397.x.

Kumar, P., R. Kind, X. Yuan, and J. Mechie (2012), US Array receiver function images of the lithosphere-asthenosphere boundary, *Seismol. Res. Lett.*, *83*(3), 486–491, doi:10.1785/gssrl.83.3.486.

Landman, R. L., and R. M. Flowers (2013), (U-Th)/He thermochronologic constraints on the evolution of the northern Rio Grande Rift, Gore Range, Colorado and implications for rift propagation models, *Geosphere*, *9*(1), 170–187, doi:10.1130/GES00826.1.

Laughlin, A. W., M. J. Aldrich, M. Shafiqullah, and J. Husler (1986), Tectonic implications of the age, composition, and orientation of lamprophyre dikes, Navajo volcanic field, Arizona, *Earth Planet. Sci. Lett.*, *76*(3), 361–374, doi:10.1016/0012-821X(86)90087-7.

Leat, P. T., R. N. Thompson, A. N. Dickin, M. A. Morrison, and G. L. Hendry (1989), Quaternary volcanism in northwestern Colorado; implications for the roles of asthenosphere and lithosphere in the genesis of continental basalts, *J. Volcanol. Geotherm. Res.*, *37*(3), 291–310, doi:10.1016/0377-0273(89)90085-1.

Leat, P. T., A. P. Dickin, R. N. Thompson, M. A. Morrison, and G. L. Hendry (1990), Geochemistry of mafic lavas in the early Rio Grande Rift, Yarmony Mountain, Colorado, USA, *Chem. Geol.* *81*(1), 23–43, doi:10.1016/0009-2541(90)90037-8.

Leat, P. T., R. N. Thompson, M. A. Morrison, G. L. Hendry, and A. P. Dickin (1991), Alkaline hybrid mafic magmas of the Yampa area, NW Colorado, and their relationship to the Yellowstone mantle plume and lithospheric mantle domains, Contrib. *Mineral. Petrol.*, *107*(3), 310–327, doi:10.1007/BF00325101.

Lee, D.-K., and S. P. Grand (1996), Upper mantle shear structure beneath the Colorado Rocky Mountains, *J. Geophys. Res.*, *101*, 22,233–22,244, doi:10.1029/96JB01502.

Leonard, E. M. (2002), Geomorphic and tectonic forcing of late Cenozoic warping of the Colorado piedmont, *Geology*, *30*(7), 595–598, doi:10.1130/0091–7613(2002)030<0595:gatfol>2.0.co;2.

Lester, A., and G. L. Farmer (1998), Lower crustal and upper mantle xenoliths along the Cheyenne Belt and vicinity, *Rocky Mountain Geol.*, *33*(2), 293–304, doi:10.2113/33.2.293.

Levander, A., and M. S. Miller (2012), Evolutionary aspects of lithosphere discontinuity structure in the western U.S., *Geochem. Geophys. Geosyst.*, *13*, Q0AK07, doi:10.1029/2012GC004056.

Li, A., D. W. Forsyth, and K. M. Fischer (2002), Evidence for shallow isostatic compensation of the southern Rocky Mountains from Rayleigh wave tomography, *Geology*, *30*(8), 683–686, doi:10.1130/0091–7613(2002)030<0683:EFSICO>2.0.CO;2.

Ligorria, J. P., and C. J. Ammon (1999), Iterative deconvolution and receiver-function estimation, *Bull. Seismol. Soc. Am.*, *89*(5), 1395–1400.

Lin, F.-C., and M. H. Ritzwoller (2011), Helmholtz surface wave tomography for isotropic and azimuthally anisotropic structure, *Geophys. J. Int.*, *186*(3), 1104–1120, doi:10.1111/j.1365-246X.2011.05070.x.

Lin, F.-C., B. Schmandt, and V. C. Tsai (2012), Joint inversion of Rayleigh wave phase velocity and ellipticity using US Array: Constraining velocity and density structure in the upper crust, *Geophys. Res. Lett.*, *39*, L12303, doi:10.1029/2012GL052196.

Lipman, P. W. (2007), Incremental assembly and prolonged consolidation of Cordilleran magma chambers: Evidence from the Southern Rocky Mountain volcanic field, *Geosphere*, *3*(1), 42–70, doi:10.1130/ges00061.1.

Liu, L., and M. Gurnis (2010), Dynamic subsidence and uplift of the Colorado Plateau, *Geology*, *38*(7), 663–666, doi:10.1130/g30624.1.

Lowry, A. R., and M. Perez-Gussinye (2011), The role of crustal quartz in controlling Cordilleran deformation, *Nature*, *471*(7338), 353–357, doi:10.1038/nature09912.

Lowry, A. R., N. M. Ribe, and R. B. Smith (2000), Dynamic elevation of the Cordillera, western United States, *J. Geophys. Res.*, *105*, 23,371–323,390, doi:10.1029/2000JB900182.

MacCarthy, J. R. (2011), Lithospheric structure beneath the southern Rocky Mountains and support for high elevations, PhD thesis, N. M. Inst. of Mining and Technol., Socorro, N. M.

Magnani, M. B., K. C. Miller, A. Levander, and K. Karlstrom (2004), The Yavapai-Mazatzal boundary; a long-lived tectonic element in the lithosphere of southwestern North America, *GSA Bull.*, *116*, 1137–1142, doi:10.1130/B25414.1.

McCallum, M. E., C. D. Mabarak, and H. G. Coopersmith (1979), Diamonds from Omberlites in the Colorado-Wyoming state line district, in *Kimberlites, Diatremes, and Diamonds: Their Geology, Petrology, and Geochemistry*, edited by F. R. Boyd and H.O.A. Meyer, pp. 42–58, AGU, Washington, D. C.

McKenzie, D. (1989), Some remarks on the movement of small melt fractions in the mantle, *Earth Planet. Sci. Lett.*, *95*(1), 53–72, doi:10.1016/0012-821X(89)90167-2.

McMillan, M. E., C. L. Angevine, and P. L. Heller (2002), Postdepositional tilt of the Miocene-Pliocene Ogallala group on the western Great Plains: Evidence of late Cenozoic uplift of the Rocky Mountains, *Geology*, *30*(1), 63–66, doi:10.1130/0091–7613(2002)030<0063:PTOTMP>2.0.CO;2.

McMillan, M. E., P. L. Heller, and S. L. Wing (2006), History and causes of post-Laramide relief in the Rocky Mountain orogenic plateau, *GSA Bull.*, *118*, 393–405, doi:10.1130/b25715.1.

Mercier, J. P., M. Bostock, and A. M. Baig (2006), Improved Green's functions for passive source structural studies, *Geophysics*, *71*(4), SI95–SI102, doi:10.1190/1.2213951.

Morozova, E. A., X. Wan, K. R. Chamberlain, S. B. Smithson, R. Johnson, and K. E. Karlstrom (2005), Inter-wedging nature of the Cheyenne belt: Archean-Proterozoic suture defined by seismic reflection data, in *The Rocky Mountain Region—An Evolving Lithosphere: Tectonics, Geochemistry, and Geophysics, Geophys. Monogr. Ser.,* vol. 154, edited by K. E. Kalstrom and G. R. Keller, pp. 217–226, AGU, Washington, D. C., doi:10.1029/154GM15.

Moucha, R., A. M. Forte, D. B. Rowley, J. X. Mitrovica, N. A. Simmons, and S. P. Grand (2008), Mantle convection and the recent evolution of the Colorado Plateau and the Rio Grande Rift valley, *Geology*, *36*(6), 439–442, doi:10.1130/g24577a.1.

Nagy, D., G. Papp, and J. Benedek (2000), The gravitational potential and its derivatives for the prism, *J. Geod.*, *74*, 552–560, 10.1007/s001900000116.

Obrebski, M., R. M. Allen, F. Pollitz, and S.-H. Hung (2011), Lithosphere–asthenosphere interaction beneath the western United States from the joint inversion of body-wave traveltimes and surface-wave phase velocities, *Geophys. J. Int.*, *185*(2), 1003–1021, doi:10.1111/j.1365-246X.2011.04990.x.

Penn, B. S., and D. A. Lindsey (2009), 40Ar/ 39Ar dates for the Spanish Peaks intrusions in south-central Colorado, *Rocky Mountain Geol.*, *44*(1), 17–32.

Putirka, K. (2008), Excess temperatures at ocean islands; implications for mantle layering and convection, *Geology*, *36*(4), 283–286, doi:10.1130/G24615A.1.

Rau, C. J., and D. W. Forsyth (2011), Melt in the mantle beneath the amagmatic zone, southern Nevada, *Geology*, *39*(10), 975–978, doi:10.1130/g32179.1.

Reed, J. C. Jr., M.E. Bickford, W. R. Premo, J. N. Aleinikokk, and J. S. Pallister (1987), Evolution of the Early Proterozoic Colorado province: Constraints from U-Pb geochronology, *Geology*, *15*(9), 861–865, doi:10.1130/0091-7613(1987)15<861:EOTEPC>2.0.CO;2.

Reiter, M. (2008), Geothermal anomalies in the crust and upper mantle along Southern Rocky Mountain transitions, *GSA Bull.*, *120*, 431–441, doi:10.1130/B26198.1.

Riihimaki, C. A., R. S. Anderson, and E. B. Safran (2007), Impact of rock uplift on rates of late Cenozoic Rocky Mountain river incision, *J. Geophys. Res.*, *112*, F03S02, doi:10.1029/2006JF000557.

Riter, J. C. A., and D. Smith (1996), Xenolith constraints on the thermal history of the mantle below the Colorado Plateau, *Geology*, *24*(3), 267–270, doi:10.1130/0091-7613(1996)024<0267:xcotth>2.3.co;2.

Roy, M., S. Kelley, F. J. Pazzaglia, S. Cather, and M. A. House (2004), Middle Tertiary buoyancy modification and its relationship to rock exhumation, cooling, and subsequent extension at the eastern margin of the Colorado Plateau, *Geology*, *32*(10), 925–928, doi:10.1130/G20561.1.

Rychert, C. A., K. M. Fischer, and S. Rondenay (2005), A sharp lithosphere-asthenosphere boundary imaged beneath eastern North America, *Nature*, *436*(7050), 542–545, doi:10.1038/nature03904.

Rychert, C. A., S. Rondenay, and K. M. Fischer (2007), P-to-S and S-to-P imaging of a sharp lithosphere-asthenosphere boundary beneath eastern North America, *J. Geophys. Res.*, *112*, B08314, doi:10.1029/2006JB004619.

Rychert, C. A., P. M. Shearer, and K. M. Fischer (2010), Scattered wave imaging of the lithosphere-asthenosphere boundary, *Lithos*, *120*(1), 173–185, doi:10.1016/j.lithos.2009.12.006.

Satsukawa, T., K. Michibayashi, E. Y. Anthony, R. J. Stern, S. S. Gao, and K. H. Liu (2011), Seismic anisotropy of the uppermost mantle beneath the Rio Grande rift: Evidence from Kilbourne Hole peridotite xenoliths, New Mexico, *Earth Planet. Sci. Lett.*, *311*, 172–181, doi:10.1016/j.epsl.2011.09.013.

Schmandt, B., and E. Humphreys (2010), Complex subduction and small-scale convection revealed by body-wave tomography of the western United States upper mantle, *Earth Planet. Sci. Lett.*, *297*(3), 435–445, doi:10.1016/j.epsl.2010.06.047.

Schutt, D. L., and C. E. Lesher (2006), Effects of melt depletion on the density and seismic velocity of garnet and spinel lherzolite, *J. Geophys. Res*, *111*, B05401, doi:10.1029/2003jb002950.

Shapiro, N. M., and M. Campillo (2004), Emergence of broadband Rayleigh waves from correlations of the ambient seismic noise, *Geophys. Res. Lett.*, *31*, L07614, doi:10.1029/2004GL019491.

Shaw, C. A., and K. E. Karlstrom (1999), The Yavapai-Mazatzal crustal boundary in the Southern Rocky Mountains, *Rocky Mountain Geol.*, *34*(1), 37–52, doi:10.2113/34.1.37.

Sheehan, A. F., G. A. Abers, C. H. Jones, and A. L. Lerner-Lam (1995), Crustal thickness variations across the Colorado Rocky Mountains from teleseismic receiver functions, *J. Geophys. Res.*, *100*, 20,391–320,404, doi:10.1029/95JB01966.

Shen, W., M. H. Ritzwoller, and V. Schulte-Pelkum (2013), A 3-D model of the crust and uppermost mantle beneath the central and western US by joint inversion of receiver functions and surface wave dispersion, *J. Geophys. Res.*, *118*(1), 262–272, doi:10.1029/2012JB009602.

Smith, D. (2010), Antigorite peridotite, metaserpentinite, and other inclusions within diatremes on the Colorado Plateau, SW USA: implications for the mantle wedge during low-angle subduction, *J. Petrol.*, *51*(6), 1355–1379, doi:10.1093/petrology/egq022.

Snelson, C. M., T. J. Henstock, G. R. Keller, K. C. Miller, and A. Levander (1998), Crustal and uppermost mantle structure along the Deep Probe seismic profile, *Rocky Mountain Geol.*, *33*(2), 181–198, doi:10.2113/33.2.181.

Stachnik, J. C. (2010), Seismic imaging of crust and upper mantle structure in western North America via surface wave inversion and wavefield depropagation, PhD thesis, Univ. of Wyoming, Laramie, Wyo.

Stachnik, J. C., K. Dueker, D. L. Schutt, and H. Yuan (2008), Imaging Yellowstone plume-lithosphere interactions from inversion of ballistic and diffusive Rayleigh wave dispersion and crustal thickness data, *Geochem. Geophys. Geosyst.*, *9*, Q06004, doi:10.1029/2008GC001992.

Stixrude, L., and C. Lithgow-Bertelloni (2005), Mineralogy and elasticity of the oceanic upper mantle: Origin of the low-velocity zone, *J. Geophys. Res*, *110*, B03204, doi:10.1029/2004jb002965.

Takei, Y. (2000), Acoustic properties of partially molten media studied on a simple binary system with a controllable dihedral angle, *J. Geophys. Res.*, *105*, 16,665–16,682, doi:10.1029/2000JB900124 .

Thompson, R. N., P. T. Leat, A. P. Dickin, M. A. Morrison, G. L. Hendry, and S. A. Gibson (1990), Strongly potassic mafic magmas from lithospheric mantle sources during continental extension and heating; evidence from Miocene minettes of Northwest Colorado, U.S.A, *Earth Planet. Sci. Lett.*, *98*(2), 139–153, doi:10.1016/0012-821X(90)90055-3.

Thompson, R. N., D. Velde, P. T. Leat, M. A. Morrison, J. G. Mitchell, A. P. Dickin, and S. A. Gibson (1997), Oligocene lamproite containing an Al-poor, Ti-rich biotite, Middle Park, Northwest Colorado, USA, *Minera. Mag.*, *61*(4), 557–572.

Turcotte, D. L., and G. Schubert (2002), *Geodynamics*, Cambridge Univ. Press, Cambridge, U. K.

Tweto, O. (1979), The Rio Grande rift system in Colorado, in *Rio Grande Rift: Tectonics and Magmatism*, edited by R. E. Riecker, pp. 33–56, AGU, Washington, D. C.

Tweto, O., and P. K. Sims (1963), Precambrian ancestry of the Colorado mineral belt, *GSA Bull.*, *74*(8), 991–1014, doi:10.1130/0016-7606(1963)74[991:PAOTCM]2.0.CO;2.

VanDecar, J. C., and R. S. Crossen, (1990), Determination of teleseismic relative phase velocity arrival times using multi-channel cross-correlation and least squares, *Bull. Seismol. Soc. Am.*, *80*(1), 150–169.

van Wijk, J. W., W. S. Baldridge, J. van Hunen, S. Goes, R. Aster, D. D. Coblentz, S. P. Grand, and J. Ni (2010), Small-scale convection at the edge of the Colorado Plateau; implications for topography, magmatism, and evolution of Proterozoic lithosphere, *Geology*, *38*(7), 611–614, doi:10.1130/G31031.1.

Wannamaker, P. E., et al. (2008), Lithospheric dismemberment and magmatic processes of the Great Basin-Colorado Plateau transition, Utah, implied from magnetotellurics, *Geochem. Geophys. Geosyst.*, *9*, Q05019, doi:10.1029/2007gc001886.

Watts, A. B. (2001), *Isostasy and Flexure of the Lithosphere*, Cambridge Univ. Press, Cambridge, U. K.

West, M., J. Ni, W. S. Baldridge, D. Wilson, R. Aster, W. Gao, and S. Grand (2004), Crust and upper mantle shear-wave structure of the Southwest United States: Implications for rifting and support for high elevation, *J. Geophys. Res.*, *109*, B03309, doi:10.1029/2003JB002575.

Whitmeyer, S. J., and K. E. Karlstrom (2007), Tectonic model for the Proterozoic growth of North America, *Geosphere*, *3*(4), 220–259, doi:10.1130/ges00055.1.

Wilson, D. C., D. A. Angus, J. F. Ni, and S. P. Grand (2006), Constraints on the interpretation of S-to-P receiver functions, *Geophys. J. Int.*, *165*(3), 969–980, doi:10.1111/j.1365-246X.2006.02981.x.

Wölbern, I., G. Rümpker, K. Link, and F. Sodoudi (2012), Melt infiltration of the lower lithosphere beneath the Tanzania craton and the Albertine rift inferred from S receiver functions, *Geochem. Geophys. Geosyst.*, *13*, Q0AK08, doi:10.1029/2012GC004167.

Yang, Y., D. W. Forsyth, and D. S. Weeraratne (2007), Seismic attenuation near the East Pacific Rise and the origin of the low-velocity zone, *Earth Planet. Sci. Lett.*, *258*(1), 260–268, doi:10.1016/j.epsl.2007.03.040.

Yuan, X., R. Kind, X. Li, and R. Wang (2006), The S receiver functions; synthetics and data example, *Geophys. J. Int.*, *165*(2), 555–564, doi:10.1111/j.1365-246X.2006.02885.x.

Yuan, H., B. Romanowicz, K. M. Fischer, and D. Abt (2011), 3-D shear wave radially and azimuthally anisotropic velocity model of the North American upper mantle, *Geophys. J. Int.*, *184*(3), 1237–1260, doi:10.1111/j.1365-246X.2010.04901.x.

Zhu, L. P., and H. Kanamori (2000), Moho depth variation in southern California from teleseismic receiver functions, *J. Geophys. Res.*, *105*, 2969–2980, doi:10.1029/1999JB900322.

Zoback, M. L., and W. D. Mooney (2003), Lithospheric buoyancy and continental intraplate stresses, *Int. Geol. Rev.*, *45*(2), 95–118, doi:10.2747/0020-6814.45.2.95.